THE DE HAAS-VAN ALPHEN EFFECT IN ANTIMONY-TIN ALLOYS

THE DE HAAS-VAN ALPHEN EFFECT IN ANTIMONY-TIN ALLOYS

By

ALLEN EDWARD DUNSWORTH, M.Sc.

A Thesis
Submitted to the Faculty of Graduate Studies
in Partial Fulfilment of the Requirements
for the Degree
Doctor of Philosophy

McMaster University
September 1972

DOCTOR OF PHILOSOPHY (1972)
(Physics)

MCMASTER UNIVERSITY
Hamilton, Ontario.

TITLE: The de Haas-van Alphen Effect in Antimony-Tin alloys.

AUTHOR: Allen Edward Dunsworth, B.Sc. (Dalhousie) M.Sc. (Dalhousie)

SUPERVISOR: Dr. W.R. Datars

NUMBER OF PAGES: viii, 78

SCOPE AND CONTENTS:

The Fermi surfaces of antimony and its alloys with up to 0.29 atomic percent tin are studied using the de Haas-van Alphen effect. Several models for the conduction and valence bands are compared with experiment. The alloying behaviour is considered with reference to both rigid and non-rigid band pictures. Reasonable agreement is obtained with the rigid band model

ABSTRACT

The de Haas-van Alphen effect has been used to measure the Fermi surface areas, cyclotron masses and Dingle temperatures in antimony and its alloys containing less than 0.3 percent tin. The Fermi surface of each alloy was similar to the pure antimony surface. However the hole surface increased in size and the electron surface shrunk since tin removes electrons from the alloy. The cyclotron masses increased and decreased for holes and electrons respectively, giving a definite indication of non-parabolic conduction and valence bands. The cyclotron masses were found from the temperature dependence of the dHvA amplitude after interfering dHvA frequency components were removed by a Fourier analysis technique. The Dingle temperature increased roughly linearily with tin concentration.

A comparison of the hole and electron Fermi surface volumes with the number of tin atoms added to the alloys shows that one tin atom removes one electron from the alloy as expected from the unit valence difference between antimony and tin. This value is higher than that found by other workers using different techniques.

The shapes of the energy bands along with the cyclotron masses have been compared with several band models. An ellipsoidal band provides a rough overall description of both holes and electrons while an ellipsoidal nonparabolic band describes the mass behaviour on alloying more accurately. A pseudopotential band calculated using the method and potential of Falicov and Lin (1967) was also compared with the data.

The observed relative frequency changes were used to compare the data with the rigid band model of alloying. The bands are rigid for low concentrations. At higher concentrations there are deviations apparently caused by the cyclotron mass change and an axial ratio change in the hole Fermi surface.

ACKNOWLEDGEMENTS

I wish to express my thanks to my supervisor, Dr. W. R. Datars, for his advice and assistance during the course of the work and during the writing of this thesis. I also wish to thank the members of the Fermi surface group for their helpful suggestions, particularly Mr. C.A. Verge who assisted with many technical problems.

This research was supported through grants from the National Research Council of Canada and the Defense Research Board of Canada. Personal financial support from McMaster University and the National Research Council of Canada is gratefully acknowledged.

TABLE OF CONTENTS

		Page
CHAPTER I	INTRODUCTION	1
CHAPTER II	THEORETICAL BACKGROUND	4
	A. de Haas-van Alphen Effect	4
	B. Energy Bands and Fermi Surfaces	7
	C. Alloys	12
CHAPTER III	METHOD AND APPARATUS	16
CHAPTER IV	PROPERTIES OF MATERIALS	20
	A. Properties of Antimony	20
	B. Properties of Antimony-Tin Alloys	26
CHAPTER V	PREPARATION OF ALLOYS	29
CHAPTER VI	EXPERIMENTAL RESULTS	35
CHAPTER VII	DISCUSSION	57
	A. Rigid Band Model	57
	B. Band Shapes	61
	C. Nonrigid Bands	70
CHAPTER VIII	CONCLUSIONS	72
BIBLIOGRAPHY		74

LIST OF FIGURES

Figure Numbers Page

1. Block diagram of dHvA apparatus 18
2. First Brillouin zone of Antimony 22
3. Phase diagram of antimony-tin 25
4. dHvA frequencies for pure antimony 36
5. dHvA frequencies for 0.034 wt.% tin 37
6. dHvA frequencies for 0.17 wt.% tin 38
7. dHvA frequencies for 0.22 wt.% tin 39
8. dHvA frequencies for 0.23 wt.% tin 40
9. dHvA frequencies for 0.28 wt.% tin 41
10. dHvA frequencies for holes (all concentrations) 44
11. dHvA frequencies for electrons (all concentrations) 45
12. Principal maximum and minimum frequencies as a function of concentration. 46
13. a) two dHvA Fourier peaks
    b) one Fourier peak after filtering
    c) cyclotron mass of pure antimony
    d) cyclotron mass of 0.23 at.% tin alloy 50
14. Concentration dependence of hole and electron minima cyclotron masses 53
15. Relative frequency shift with concentration 59
16. Cyclotron mass versus frequency plot for non-parabolic bands. 63
17. Pseudopotential hole grid in a mirror plane 65
18. Pseudopotential electron grid in a mirror plane 66

LIST OF TABLES

Table Numbers		Page
I	Room temperature lattice parameters of antimony-tin solid solution	26
II	Tin concentration of alloys	33
III	Summary of experimental data for antimony-tin alloys	42
IV	Summary of carrier concentrations in antimony-tin alloys	56
V	Summary of results of pseudopotential calculations	68

CHAPTER I

INTRODUCTION

The de Haas-van Alphen (dHvA) effect is a useful tool to study the Fermi surface properties of a pure metal or alloy. The dHvA frequencies give directly the extremal cross-sectional areas of the Fermi surface while the temperature and magnetic field dependence allow the cyclotron mass and Dingle temperature to be found. If the areas, cyclotron masses and Dingle temperatures are known over the entire Fermi surface, then, in certain circumstances the radius vector, velocity vector and scattering time can be found for any point on the Fermi surface.

The problem of alloys is an interesting and natural extension of the large amount of experimental and theoretical work done in pure metals over the last twenty years. An alloy differs from a pure metal mainly by the greater number of impurity scattering centers introduced into it. These scattering centers destroy the periodicity of the crystal lattice and broaden the electron states. One of the main results of alloy studies has been to show that in spite of the destruction of the periodicity, alloys still behave in the same way as do pure metals, although the increased scattering time often makes experimental measurements much more difficult.

The present work was undertaken to determine how the Fermi surface of antimony alloyed with a small amount of tin differed from the pure antimony Fermi surface and whether the differences observed were in agreement with theories of alloying, particularly the rigid band theory. Previously, galvanomagnetic studies have been made on antimony alloys with less than 0.8% tin (Epstein and Juretschke 1963) and for concentrations between 2 and 8% tin (Saunders and Oktu 1968). Also Ishizawa and Tanuma (1965) have made dHvA measurements on 0.1% Sn alloy. These authors indicated that the band shapes do not change greatly with alloying. The Fermi surface increased and decreased for holes and electrons respectively. However, such measurements were not very sensitive to the detailed shape of a Fermi surface, in contrast to the high sensitivity to shape of a detailed dHvA experiment. This previous work suggested that only 0.3 electrons per atom were removed by adding tin, a value much smaller than the valence difference of one between antimony and tin. Theoretically such a large discrepancy was not expected.

Chapter II provides a theoretical background of the dHvA effect along with a description of energy bands and Fermi surfaces in both pure metals and alloys. Chapter III describes the experimental techniques and apparatus necessary to measure a dHvA signal. Chapter IV gives a detailed background discussion of pure antimony and its Fermi surface and also of antimony-tin alloys and their properties. The preparation of alloys and experimental results are considered in Chapters V and VI while in Chapter VII comparisons of experiment are made with alloy theories and band shapes expected from theory. Chapter VIII contains the conclusions of the study.

CHAPTER II

THEORETICAL BACKGROUND

A. The dHvA Effect

The dHvA effect is an oscillatory variation in the magnetization of a metal as a function of magnetic field H. In general, a pure metal single crystal, temperatures below 20°K and magnetic fields of the order of 10 kG are needed to observe the effect. In a magnetic field, the electrons populate quantized energy levels called Landau levels. The separation of the Landau levels depends on the magnetic field. The effect arises from the emptying of the Landau levels as a level is raised above the Fermi energy, the energy above which no level is occupied. There is a change in energy of the electronic system as electrons go to levels at lower energy.

The Pauli exclusion principle prevents more than one electron from occupying any quantum state. Since the energy available to an electron at low temperature is very small, only those electrons that lie quite near the Fermi level can change their states by moving up slightly in energy to occupy an empty state above the Fermi level. These electrons give rise to all the low temperature properties measured with the dHvA effect. Since a magnetic field exerts no force in the direction parallel to the field, the orbit of each electron occurs in a plane perpendicular to the field. The magnetic field cannot change the energy of an electron so an orbit occurs only at the Fermi energy, thereby tracing out a path on the Fermi surface. Usually the orbits are closed, meaning the electron repeats the same path many times, but this need not be true in all cases. Open orbits exist but cannot be detected with the dHvA effect. As the crystal is rotated in the magnetic field, the orbits change shape and size. The dHvA effect measures directly the extremal cross-sectional areas perpendicular to the field of each orbit. By knowing the cross-sectional areas of the Fermi surface at different angles in the crystal, the entire shape of the Fermi surface can often be deduced.

The full expression for the oscillatory magnetization is (in spherical polar coordinates) (Lifshitz and Kosevich 1955, Gold 1968 for a review)

$$\begin{aligned}
\bar{M}_i = &- \frac{e\hbar\, A_i}{4\pi^4 m_i^*} \left(\frac{2\pi e H}{\hbar}\right)^{1/2} \left|\frac{\partial^2 A_i}{\partial k_H^2}\right|^{-1/2} \\
&\times \left[\hat{H} - \frac{1}{F_i}\frac{\partial F_i}{\partial \theta}\,\hat{\theta} - \frac{1}{F_i \sin\theta}\frac{\partial F_i}{\partial \phi}\,\hat{\phi}\right] \\
&\times \Big[\sum_{r=1}^{\infty} \frac{1}{r^{3/2}} \left(\frac{2\pi^2 r m_i^* k_B T}{e\hbar H}\right) \exp\left(\frac{-2\pi^2 r m_i^* k_B T_D}{e\hbar H}\right) \\
&\qquad \times 1/\sinh\left(\frac{2\pi^2 r m_i^* k_B T}{e\hbar H}\right) \\
&\times \sin\left(2\pi r\left[\frac{F_i}{H} - \gamma_i\right] \mp \frac{\pi}{4}\right) \cos\left(\frac{\pi}{2}\, r g_i \frac{m_i^*}{m}\right)\Big] \quad . \qquad (1)
\end{aligned}$$

In this equation, A_i is the extremal cross-sectional area of the Fermi surface and is related to the dHvA frequency F_i by the equation

$$F_i = \frac{\hbar}{2\pi e} A_i \quad .$$

The oscillatory term has a phase of $2\pi r(F_i/H - \gamma_i) \mp \pi/4$ so oscillations are periodic in reciprocal field. The - and + indicate a maximum or minimum cross-sectional area. m_i^* is the cyclotron mass, an electron effective mass averaged over an orbit. The cyclotron mass is defined by

$$m^* = \frac{\hbar^2}{2\pi} \frac{\partial A}{\partial E} \tag{1A}$$

so it describes the change of area for a change of energy E. The Dingle temperature T_D is a scattering parameter indicating the lifetime of an orbiting electron. It is related to the scattering time τ by

$$1/\tau = 2\pi\ k_B T_D/\hbar \quad .$$

g_i is a spin splitting factor. The term $|\partial^2 A_i/\partial k_H{}^2|$ is the curvature of the Fermi surface at the extremum. If the curvature is small, many electrons have similar orbits and the dHvA amplitude is large. If the curvature is large, the dHvA amplitude is correspondingly small. The hyperbolic sine term contains the main temperature (T) effect on the amplitude. In certain cases $1/\sinh(x) \doteq 2e^{-x}$. Then the temperature and Dingle temperature can be combined into an effective temperature $T + T_D$. The summation over r contains the harmonic content of the oscillations. Usually the fundamental (r=1) is the largest term unless the term $\cos(\frac{\pi}{2} rg_i \frac{m_i^*}{m})$ interferes by giving a spin splitting zero. In good crystals, harmonics up to 5th or 6th order can be seen quite easily. Note that the direction of $\overline{M}_i$ is not in the direction of $\overline{H}$ but is deviated to some extent by the shape of the Fermi surface as expressed in the coefficients $\frac{\partial F_i}{\partial \theta}$ and $\frac{\partial F_i}{\partial \phi}$. Only at places where these coefficients are zero is $\overline{M}_i$ parallel to the field. The subscript i is included to permit several extremal orbits to be present simultaneously. This often occurs so the total magnetization is given by

$$\overline{M} = \sum_i \overline{M}_i \quad .$$

The remaining symbols in Eq. (1) have their usual meanings.

B. Energy Bands and Fermi Surface

Having seen what can be determined experimentally from the dHvA effect, it is useful to discuss three types of energy bands and the corresponding Fermi surfaces that will be needed later. Pure metals will be considered first and then alloys.

In a metal, the simplest approximation is the free electron model. The equation of the band is

$$E = k^2$$

in atomic units (k in au, E in rydbergs). The Fermi surface is a sphere with cyclotron mass of 1 everywhere. Only the alkali metals come close to being described by this model.

However, by bringing the crystal lattice structure and potential into consideration, this simple model forms the basis of more realistic theories.

The crystal structure defines the Brillouin zone of the metal. In general the Brillouin zone boundaries intersect the Fermi sphere, so the sphere is broken up into many pieces. Each piece forms part of the new Fermi surface. The Harrison construction (Harrison 1966c)gives a procedure for building up the new Fermi surface. There are now many small and large sections of Fermi surface, each with its own dHvA frequencies. Some pieces will be holes rather than electrons. The effective masses will no longer be unity and will vary over the surface. This model called the one-OPW model has been very successful in explaining many of the complicated shapes found in different metals and is widely used as a basis for more exact calculations. Harrison (1966c) shows many Fermi surfaces of this type as a function of valence and crystal structure. In the one-OPW model, the lattice potential is not needed at all.

It is the small pieces of Fermi surface predicted by the one-OPW bands that are relevant to antimony and its alloys. Further discussion is limited to them, ignoring the large multiply connected Fermi surfaces found in some other metals. The ellipsoidal parabolic band is useful in many cases. This band has the form

$$E = \frac{k_x^2}{m_1} + \frac{k_y^2}{m_2} + \frac{k_z^2}{m_3} \qquad (2)$$

where E is the Fermi energy and $k_{x,y,z}$ are wavevector components. The Fermi surface is an ellipsoid and any cross-sectional area is an ellipse. The major and minor axes are $\sqrt{m_1 E}$, $\sqrt{m_2 E}$ and $\sqrt{m_3 E}$ and the volume is $4\pi/3\sqrt{m_1 m_2 m_3}\, E^{3/2}$. The area in the xy plane is

$$A_{xy} = \pi (m_1 m_2)^{1/2} E \tag{3}$$

and the cyclotron mass in this plane is

$$m^*_{xy} = \frac{1}{\pi}\frac{\partial A}{\partial E} = \sqrt{m_1 m_2} \quad . \tag{4}$$

The band effective masses m_1, m_2, m_3 can be found by inverting the cyclotron mass values. In antimony, this band gives a good first approximation to the actual Fermi surface for both electrons and holes.

The ellipsoidal parabolic band is modified if there is a neighbouring band having nearly the same energy. If selection rules allow the bands to interact, the two bands will repel one another making the energy gap between them larger. These bands were found in narrow gap semiconductors, where they were treated by Kane's (1957) $\overline{k}\cdot\overline{p}$ perturbation theory. The band has the form (Lax et al. 1960)

$$E + E^2/E_g = \frac{k_x^{\ 2}}{m_1} + \frac{k_y^{\ 2}}{m_2} + \frac{k_z^{\ 2}}{m_3} \quad . \tag{5}$$

The Fermi surface is still an ellipsoid, but the energy dependence is modified by the E^2/E_g term. E_g is the energy gap between the two bands. The area in the xy plane is

$$A_{xy} = \pi\sqrt{m_1 m_2}\, E(1+E/E_g) \qquad (6)$$

and the cyclotron mass is

$$m^*_{xy} = \sqrt{m_1 m_2}\,(1+2E/E_g) \quad . \qquad (7)$$

The volume is $4\pi/3\sqrt{m_1 m_2 m_3}\,(E+E^2/E_g)^{3/2}$.

Eq. (5) describes an ellipsoidal non-parabolic band.

Both the ellipsoidal, parabolic and non-parabolic bands can be changed by adding terms of 3rd and 4th order in k to describe non-ellipsoidal shapes. This introduces new parameters that must be determined from experiment. These higher order terms will not be considered except as a numerical approximation to the pseudopotential bands described later.

When the lattice potential is included along with the one-OPW Fermi surface, some one-OPW pieces may disappear and others will have their shapes and sizes changed. Pseudopotential calculations are a generalization of the one-OPW model. The pseudopotential (Harrison 1966a) is not the full ion core potential, but a reduced interaction that varies much more smoothly through the lattice. The smoothing results from the orthogonalization of the atomic core states to the valence and conduction bands in the initial description of the system. The pseudo wavefunctions have no bound states, in contrast to the real wavefunction, and interact only weakly with the lattice. The real and pseudo wavefunctions are similar in regions away from the atomic cores. The eigenenergies of the pseudowavefunction can be found quite easily by perturbation theory. Degenerate wave-functions require degenerate state perturbation theory (involving matrix diagonalization) while others can simply be treated with second order perturbation theory. The characteristic equation (Harrison 1966b)

$$|| V_{ij} - \delta_{ij}(T_{ij} - E) || = 0$$

must be solved where $T_{ij} = (\overline{k} - \overline{G}_i)^2$ is the kinetic energy, $V_{ij} = <\overline{k} - \overline{G}_i|V|\overline{k} - \overline{G}_j>$ is the potential energy and $\overline{G}_i$ are reciprocal lattice vectors. The basis states are the plane waves $|\overline{q}> = \frac{1}{\Omega} e^{i\overline{q}\cdot\overline{r}}$. $\overline{k}$ is a point in reciprocal space where the eigenenergies E are found. If the determinant is N by N, there will be N energy values for $\overline{k}$, giving N bands. Some bands may be degenerate. The size of N depends on the metal being considered. Large N gives more accurate solutions but several metals have been well described by a 2 × 2 matrix. Antimony requires a large N (89) for good convergence of the energy values (Falicov 1966). It is often sufficient to approximate the pseudopotential V_{ij} by a function which depends only on the difference of reciprocal lattice vectors $|\overline{G}_i - \overline{G}_j|$ and not on $\overline{k}$ (local pseudopotential). This local approximation has been quite successful in practice for a number of metals. Harrison (1966) and Cohn and Heine (1970) give useful insight and information on the general properties of pseudopotentials and their application to predictions of many different properties of metals.

C. Alloys

Only binary, substitutional alloys, or solid solutions will be discussed. In these alloys, an impurity atom replaces a host atom on the host site. It is assumed that the replacement is random, so no regions unusually high in impurity concentration are formed. There are small charges from the pure host lattice parameters as the concentration increases and local strains around each impurity, but there are no new phases formed.

Consider the effect of adding an impurity atom with valence difference Z from the host. If N is the number of impurities added then ZN electrons are gained or lost depending on the sign of Z. Since the Fermi level defines the boundary between occupied and unoccupied states, changing N raises or lowers the Fermi level. The rigid band model (Heine 1954) assumes that the energy bands of the alloy are the same as those of the host but the Fermi energy is shifted. The changed Fermi level exposes new regions of the host energy bands to study. In this way, the energy dependence of the bands can be found.

The band overlap energy is the energy difference between the top of the hole band and the bottom of the electron band. It is the sum of the electron and hole Fermi energies if both are considered positive. If the individual band shapes are kept the same, but the overlap energy is allowed to vary (Heine 1954), then this gives deviations from the rigid band model. More complicated departures from the rigid band theory involve both overlap energy shifts and shape changes. The combined effect is considered in the pseudopotential description.

The pseudopotential formulation allows the changes of lattice parameters to be included in a straightforward way and also permits the pseudopotential itself to be adjusted to account for the impurities added. The same procedure outlined for the pseudopotential calculation of a pure metal is used with the correct values for lattice parameters and pseudopotential change. A full band calculation is usually required for each alloy

The pseudopotential appropriate for a metal atom transplanted to another lattice depends only on the ratio of the atomic volume Ω and dielectric constant $\varepsilon(q)$ for the original and final lattices (Cohen 1970b). If the old lattice is A and the new lattice is B, then

$$V(\text{A in B}) = \frac{\Omega_A \varepsilon_A(q)}{\Omega_B \varepsilon_B(q)} \; V(\text{A in A}) \quad . \tag{8}$$

The atomic volume term results from normalization, while the dielectric constant comes from the requirements of screening. There is a tabulation of pseudopotentials and atomic volumes by Cohen (1970a). The dielectric constants can be calculated from the carrier density. The pseudopotential of the alloy is an average over the host and impurity atoms (Harrison 1966d). If B is the host then

$$V = (1-c)V(B \text{ in } B) + cV(A \text{ in } B) \qquad (9)$$

where c is the atomic concentration. This is correct if c is small. If c is large then V(B in B) should be corrected for the change of dielectric constant. If the host and impurity are similar, the alloy pseudopotential will nearly be the same as the host pseudopotential. For 1% tin in antimony, the alloy pseudopotential is only about .1% different from the antimony value. In the antimony-tin alloys, the change of lattice parameter on alloying causes a larger effect than the pseudopotential difference.

Another way of looking at the alloy problem is to consider scattering from the impurities. If, for simplicity, there is only one impurity in a region of radius R, with R being large with respect to impurity potential range, then the effect of adding the impurity is to change the boundary condition of the wavefunction at R (Kittel 1963a). If the wavefunctions are written as partial waves as is customary in scattering theory, then there is a phase shift η between the old (k') and new (k) boundary conditions of the form

$$kR + \eta = k'R \quad .$$

If η is small, then the energy shift at any point in k space is

$$\Delta E_R = \langle k|V_P|k\rangle \tag{10}$$

from the Born approximation which gives the rigid band model if ΔE_R is not a function of $\overline{k}$ (Kittel 1963a). In general, η is not small so an exact numerical solution must be used rather than the Born approximation. This is related to the screening since each impurity must be surrounded by an electron cloud which shields the impurity potential at large distances. The Friedel sum rule given below describes the phase shifts η_L necessary to provide this screening for an impurity of valence difference Z.

$$Z = \frac{2}{\pi} \sum_L (2L+1)\eta_L(k_F) \tag{11}$$

η_L is often negligible for L>2 or 3. If the potential is known, η_L can be directly calculated from the Schrodinger equation.

CHAPTER III

METHOD AND APPARATUS

The low-frequency modulation method (Poulsen 1971) was used to detect the dHvA signal. This method requires a small, alternating current magnetic field to be applied to the sample along with the main field $\overline{H}_o$. Then the magnetic field at any time can be written as

$$\overline{H}(t) = \overline{H}_o + \overline{h} \sin\omega t \qquad (12)$$

where $\overline{h}$ is the amplitude of the fluctuating field and ω is its angular frequency. If the Lifshitz-Kosevich expression (Eq. 1) for the magnetization is written as

$$\overline{M} = \overline{A}(\overline{H}) \sin(2\pi F/|\overline{H}| + \phi) \qquad (13)$$

then substituting Eq. (12) into Eq. (13) gives (after using the fact that $|\overline{H}_o|>>|\overline{h}|$,

$$\cos(x \sin\theta) = J_o(x) + 2 \sum_{N=1}^{\infty} J_{2N}(x) \cos(2N\theta)$$

and

$$\sin(x \sin\theta) = 2 \sum_{N=0}^{\infty} J_{2N+1}(x) \sin([2N+1]\theta))$$

for the time derivative of $\overline{M}$ the series

$$\frac{\partial\overline{M}}{\partial t} = -\overline{A}(H) \sum_{n=1}^{\infty} 2n\omega J_n(\lambda)\sin(n\omega t+n\pi/2)$$

$$\times \sin(\frac{2\pi F}{H_o} + \phi + \frac{n\pi}{2}) \qquad (14)$$

where $\lambda = \frac{2\pi Fh}{H_o^2}$ (Gold 1968a). The value of λ given here only applies if $\bar{h}||\bar{H}_o$ as occurs in this experiment. If this is not the case, see Gold (1968a). Thus the time derivative of $\bar{M}$ is a series of harmonics of the modulation frequency. If $\bar{H}_o$ is changed slowly with time (as compared with ω) then each harmonic is modulated by a frequency characteristic of the dHvA frequency F and the magnetic field sweep speed.

The apparatus is shown in block form in Fig. 1. The harmonics are integral multiples of 517 Hz. This frequency is low enough to allow nearly complete penetration of the sample by the modulation field. If this is not true, then the expression for the amplitude, but not the frequency, in Eq. (14) is modified (Gold 1968b). One harmonic is chosen by filters in the detection system and this harmonic is demodulated by a phase sensitive detector driven at the harmonic frequency followed by a low pass filter. All the measurements reported were made at the second harmonic frequency (1034 Hz). Since A and λ are slowly varying functions of H_o, the final output is a low frequency sinusoid with a field dependent amplitude. In general, there are several different frequencies present, so the oscillations are recorded digitally on magnetic tape along with the magnetic field values. These data are then Fourier analyzed to find the frequency components. In practice, the signal to noise ratio and the resolution allow components with amplitudes less than 1% of the largest component to be seen and frequency

Figure 1 Block diagram of experimental system

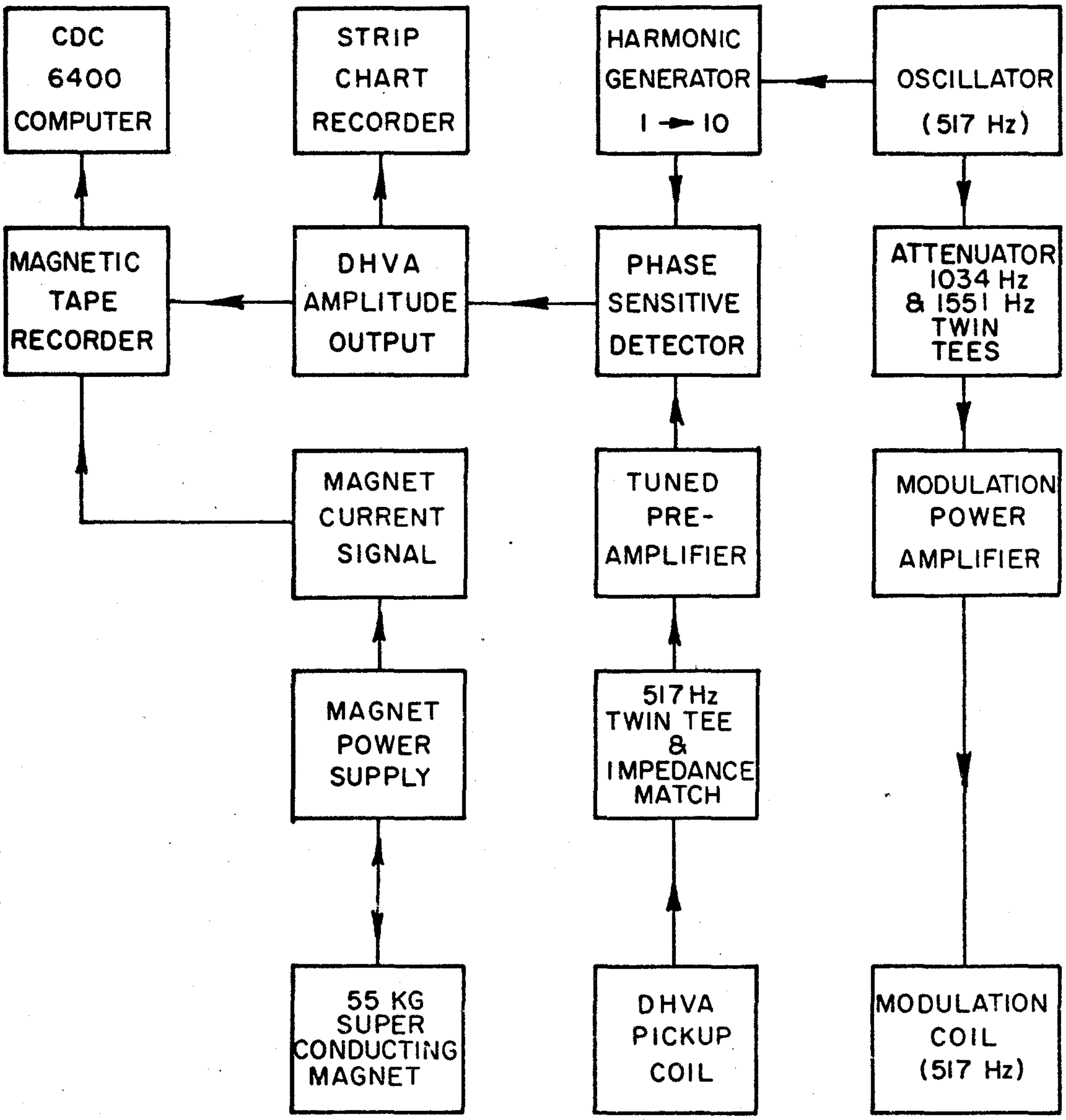
CDC 6400 COMPUTER
STRIP CHART RECORDER
HARMONIC GENERATOR 1 → 10
OSCILLATOR (517 Hz)
MAGNETIC TAPE RECORDER
DHVA AMPLITUDE OUTPUT
PHASE SENSITIVE DETECTOR
ATTENUATOR 1034 Hz & 1551 Hz TWIN TEES
MAGNET CURRENT SIGNAL
TUNED PRE-AMPLIFIER
MODULATION POWER AMPLIFIER
MAGNET POWER SUPPLY
517 Hz TWIN TEE & IMPEDANCE MATCH
55 KG SUPER CONDUCTING MAGNET
DHVA PICKUP COIL
MODULATION COIL (517 Hz)

separations of $\sim 1T$ to be achieved.

The driving-detection system consists of two concentric coils, the outer one to provide the modulation field (<200 gauss) and the inner one to pick up the change of magnetization of the sample inside. Each coil is split to allow the sample to be turned. The main magnetic field is provided by a 55 kG Westinghouse superconducting solenoid. The field can be driven either linearly in time or so the reciprocal field varies linearly in time. This last feature is very convenient since the dHvA oscillations are periodic in reciprocal field and not field.

The cyclotron mass was calculated from the temperature dependence of the dHvA amplitude at constant field. The temperature was found by measuring the liquid He^4 vapor pressure above the sample space with a Texas Instruments precision pressure gauge. The pressure was controlled by a Cartesian diver regulator in the pumping line. Temperatures between 4.2^oK and 1.2^oK were obtained. A discussion of the analysis required for the cyclotron mass is given in the section on experimental results.

The Dingle temperature was found from the field variation of the dHvA amplitude at constant temperature. The cyclotron mass must be found first in order to calculate the Dingle temperature. The discussion of this analysis is also postponed for a later section.

CHAPTER IV

PROPERTIES OF MATERIALS

A. Properties of Antimony

Antimony (Sb) is element number 51, a brittle, silver colored metal which crystallizes in the rhombohedral system. It has a density of 6.69 gm/cm^3, an atomic weight of 121.75 and 5 valence electrons in shells $5s^2$ and $5p^3$. Since it is a rather poor conductor of electric current, it is often referred to as a semimetal along with the related metals bismuth and arsenic.

The crystal structure is A7(rhombohedral), a structure which has a three fold axis (trigonal, T) as its highest symmetry direction. There are three mirror planes 120^o apart intersecting parallel to the trigonal axis. A two fold (binary) axis lies in each mirror plane perpendicular to the trigonal axis. A third axis perpendicular to both the binary and trigonal is usually defined and called the bisectrix axis. The antimony structure can be formed by first stretching a face centered cubic lattice along its body diagonal, thus forming a primitive cell lattice angle $\alpha < 60^o$ and then placing in each face centered cubic site a basis of two atoms pointing along the body diagonal. In a face centered cubic lattice, the primitive cell is a rhombohedron with an angle of 60^o. The separation of the two atoms is defined as 2μ

where μ is called the internal displacement parameter. If $\mu=1/4$ and $\alpha=60^{\circ}$, then the lattice is simple cubic. The lattice parameters of antimony at 4.2°K are in hexagonal coordinates: a = 4.3007Å, c = 11.222Å, u = .23362 (Barrett 1963). The rhombohedral angle α and the rhombohedral edge length a_R are found from the formulae (Wood 1963)

$$a_R^2 = \frac{a^2}{3} + \frac{c^2}{9} \text{ and } \sin(\tfrac{\alpha}{2}) = \tfrac{3}{2}(3 + (\tfrac{c}{a})^2)^{-1/2} \quad .$$

These equations give a_R = 4.4897Å and $\alpha = 57.232^{\circ}$.

It appears that the crystal structure of antimony can be understood by the band structure and lattice energy considerations of Weaire and Williams (1971) who showed that the theoretical minimum energy structure for arsenic as found from a pseudopotential calculation was in excellent agreement with experiment.

The reciprocal space structure is more useful in considering the properties of the electron bands and Fermi surfaces than is the real space structure. The first Brillouin zone is shown in Fig. 2 with important symmetry points marked with standard symbols. Since there are two atoms per unit cell, each cell contributes ten electrons and therefore the electron volume in k space is five Brillouin zones. In antimony, there is an overlap to the sixth zone so there are a small number of holes in the fifth zone along with electrons in the sixth. The A7 lattice structure, along with useful information on the reciprocal lattice vectors is described by

Figure 2 First Brillouin zone of antimony

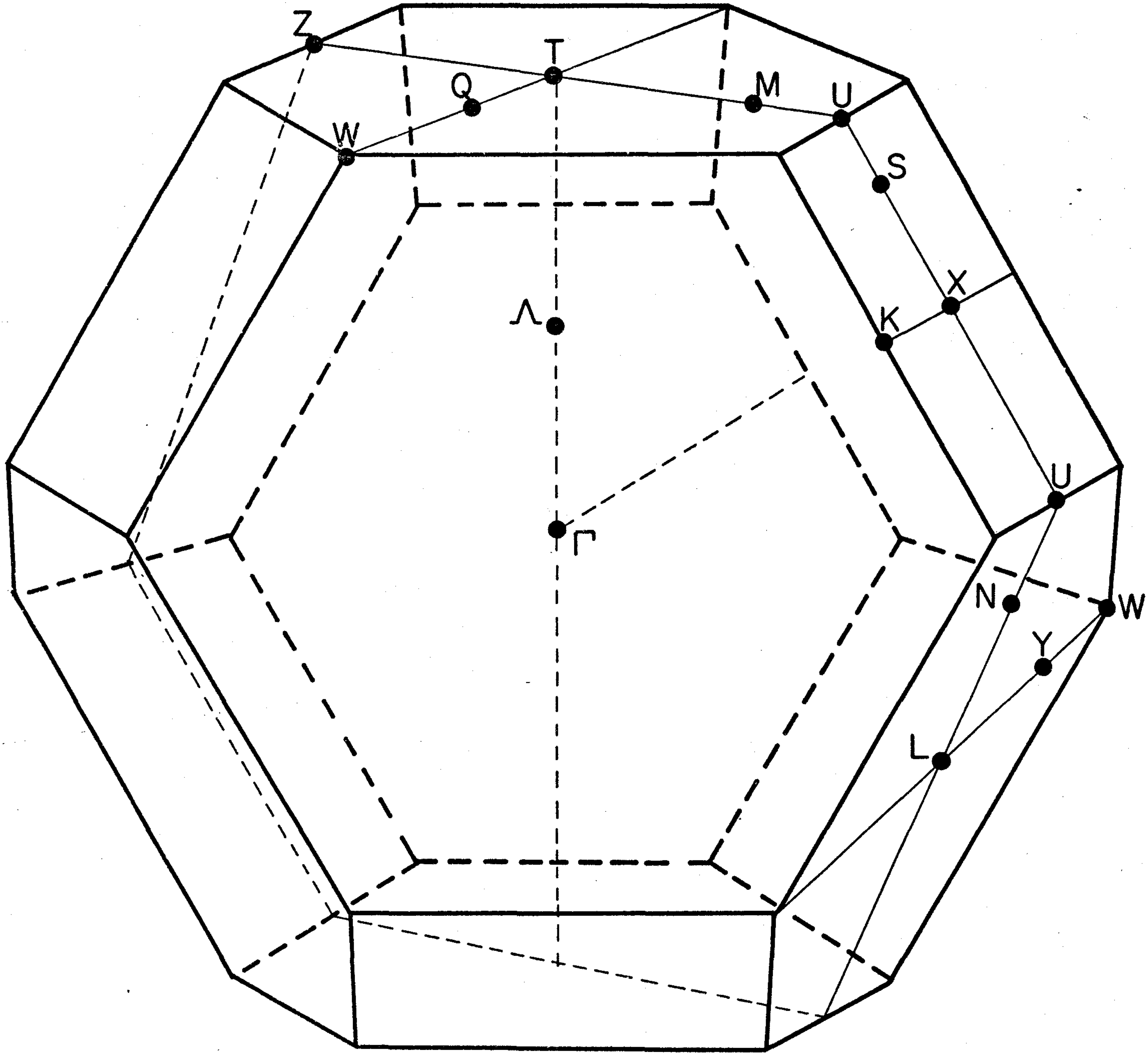
Z
T
Q
M
U
W
S
X
Λ
K
U
Γ
N
W
Y
L

Falicov and Golin (1965).

The Fermi surface of antimony has been directly studied for many years by various techniques. Some of the more recent work is mentioned below. Windmiller (1966) has made a complete study of the dHvA frequencies. His data considered along with the band structure of Falicov and Lin (1966) show that the antimony Fermi surface consists of six small hole pieces and three small electron pieces. The hole pieces are located near the T point at the point H. The only symmetry present at H is a mirror plane. The electrons are found at the L point. The electron surface has a mirror plane and also inversion symmetry. The inversion symmetry is an important feature, since without it, it is not possible to uniquely invert the dHvA frequency data to find the Fermi surface radius. The electron surface has been inverted by Ketterson and Windmiller (1970). Windmiller points out that neither electrons or holes exist in ellipsoidal pockets, but in pockets that are ellipsoids bent by about five degrees. The radio frequency size effect measurements of Herod et al. (1971) are in good agreement with the dHvA data, even to the extent that describing the hole surface as if it had inversion symmetry leads to reasonable agreement with the dHvA areas. Cyclotron masses have been found by Windmiller in his dHvA study and also by Datars and Vanderkooy (1964) using cyclotron resonance. There have been a number of galvanomagnetic studies done on antimony (Epstein and Juretschke 1963, Tanuka et al.

1968). These experiments give only indirect information on the Fermi surface. Finally, optical data of Nanney (1963) and Dresselhaus and Mavroides (1966) show various energy gaps and structure in the reflectivity in the region 0.1 to 0.5 eV. These appear to be associated with transitions occuring near the Fermi energy.

The theoretical band structure and Fermi surface of antimony has been investigated by Falicov and Lin (1966) using a local pseudopotential formulation. It was necessary for them to diagonalize an 89 by 89 matrix to get good convergence of the energy values. According to their calculations, the electrons are located at the point L while the holes are found at H. It is shown that three electron pockets and six hole pockets are sufficient to supply all the carriers required to make the number of holes and electrons equal. This equality is necessary because the lattice structure and valence make antimony a compensated metal. The areas, cyclotron masses and tilt angles of the Fermi surfaces are in reasonable agreement with experiment, especially for the electrons. The lack of inversion symmetry for the hole surface makes calculation more difficult and less accurate. There are several band gaps suggested by the theory but it is not yet clear which gaps should be associated with the gaps found experimentally. It appears that the observed transitions of $\sim$ 0.1 eV in energy cannot occur at the L and H points since the Fermi energy is greater than this energy.

Figure 3 Phase diagram of antimony-tin

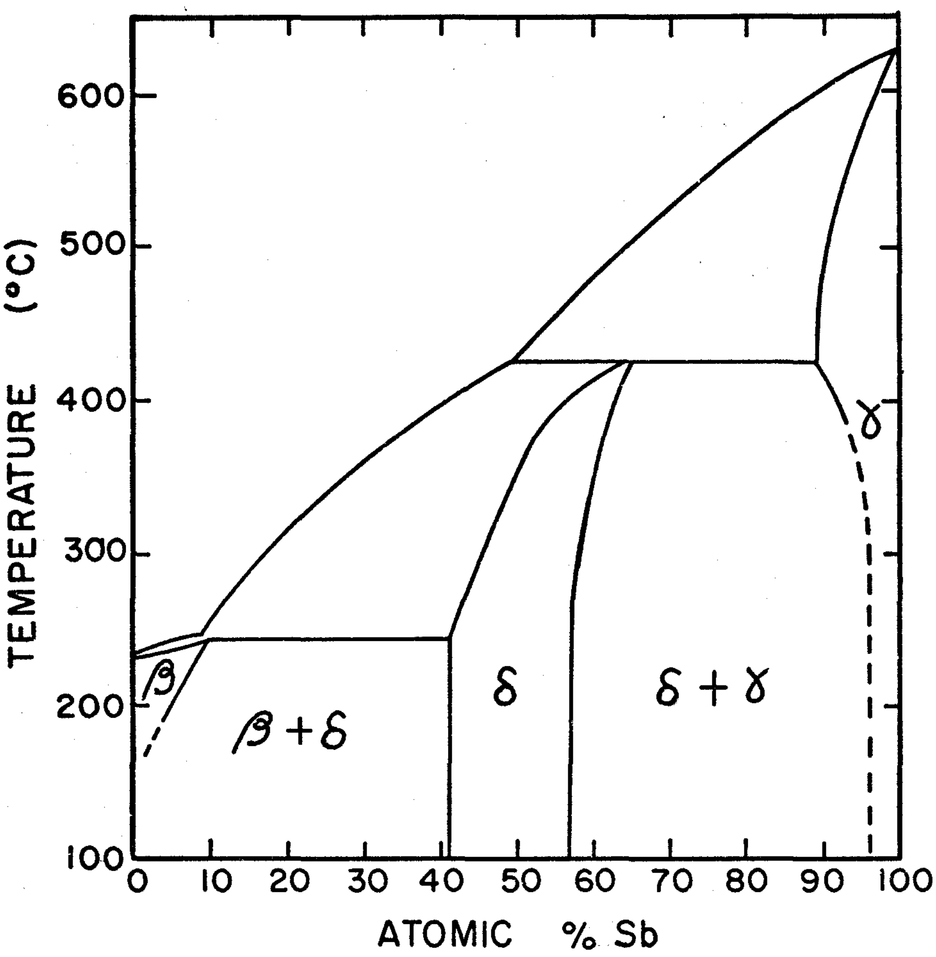
TEMPERATURE (°C)
600
500
400
300
200
100
0
10
20
30
40
50
60
70
80
90
100
ATOMIC % Sb
β
β + δ
δ
δ + γ
γ

B. Properties of Antimony - Tin Alloys

Tin (Sn) is element number 50, with an atomic weight of 118.67. The density of tin (7.31 g/cm^3) is 10% greater than that of antimony. Tin also has a different crystal structure. It is tetragonal A5 with lattice constants a = 5.83A° and c = 3.18A° and thus deviates from cubic in a different way than antimony. The valence is four, one less than that of antimony, with electrons in shells $5s^2$ and $5p^2$. Since the elements are adjacent in the periodic table, both the atomic size factor and valence difference are favorable for forming single phase solid solutions even though the crystal structure difference weighs slightly against it. The phase diagram is shown in Fig. 3. When tin is added to antimony in small amounts, the antimony crystal structure is left unchanged, but the lattice angle α and the lattice constant a_R change slightly. There are no data on the change of internal displacement parameter μ. The results of X-ray measurements by Bowen and Jones (1931) and Hagg and Hybinette (1935) are shown in Table I. These authors and standard texts

Table I

wt% Sn	rhomb. edge length A°	rhomb. angle degrees
0.0	4.506	57.08
2.0	4.521	56.65
4.0	4.528	56.53
7.0	4.532	56.22
9.5	4.540	55.96

(Hansen 1958) indicate that the solid solution limit is 9 to 10% tin. The phase diagrams as published are uncertain in this region. Above 10% there is a two phase region formed from the solid solution and the compound SbSn (see Fig. 3). One author (Ellwood) suggests the limit occurs around 3% tin. In any case, 3% is much higher than the concentrations used in the present experiment. Another point to consider is position of the phase boundary at 1°K. Galvanomagnetic studies at 77°K with alloys up to 8% tin (Saunders 1968) showed no unusual behaviour and our results do not indicate any effects of two phases at 1°K and low concentrations.

The galvanomagnetic properties of antimony with 0.2 and 0.8 at % tin were studied by Epstein and Juretschke (1963) and by Saunders and Oktu (1968) who used from 2 to 8% tin. The latter authors found an extra set of holes appearing at these high concentrations. These holes are expected on Falicov's (1966) model since pushing down the Fermi level by adding tin will expose a small hole pocket on the TW line near T. A rough calculation indicates that a few percent tin should be sufficient to produce this new pocket. There is also the possibility that the main hole pieces become connected to the smaller ones to form a Fermi surface similar to that of arsenic.

One dHvA experiment has been reported on antimony-tin alloys by Ishizawa and Tanuma (1965). These authors determined the sign of the two carrier types present in antimony by noting the frequency changes on alloying. The concentration used was nominally 0.1 at %.

A Mossbauer study was made on both the tin in antimony solid solution and the antimony in tin solution by Ruby et al. (1970). The screening of the impurity is quite high in both cases since only small changes in wavefunction were found experimentally.

CHAPTER V

PREPARATION OF ALLOYS

The alloys were grown from 99.9999% pure antimony and tin. Two methods were used to add the tin: the elements were directly mixed in the appropriate amounts or pieces of a 3% master alloy were diluted with extra antimony.

For either case, the constituents were chipped into coarse pieces and added to a vycor tube. Vycor is necessary because of the high melting point of antimony (630°C). The tube was first cleaned with an HF, HNO_3 solution and then internally coated with carbon formed by decomposing benzene with a hot flame. This carbon layer was quite durable and prevented the ingot from sticking to the tube after melting. The tube was evacuated and sometimes refilled with helium gas to reduce the evaporation of antimony. A small ring shaped heater outside the tube allowed a 1/2 in. portion of the ingot to be melted at any one time. The ingot was then zone levelled (Pfann 1966) by slowly sweeping the heater back and forth along the tube 15 or 20 times. This process is the reverse of zone refining and gives a fairly uniform concentration of tin along the ingot except for the last end that is frozen. The distribution constant k_o defined as the ratio of the concentration of tin in the solid to the concentration of tin in the liquid is $\sim$ 0.3 as estimated from the phase diagram. The sweep speed of $\sim$ 2 in/hr makes the effective k_o larger. $k_o = 1$ is the condition for most effective zone levelling. Another important parameter in this process is the total length to molten zone length ratio. The alloys were grown with this ratio between 8 and 15.

The final ingots were 4 to 5 inches long with several long parallel grains making up the bulk of the sample. Some grains showed a considerable amount of lineage, i.e., each grain consisted of several smaller crystallites misoriented with respect to one another by 1 or 2 degrees. This structure caused considerable difficulty in choosing a dHvA sample since the slight misalignment causes severe beating patterns in the dHvA frequencies, obscuring some of the desired information. Several attempts were made to seed the alloys as done by Epstein (1962). A single crystal of antimony was touched to the alloy at the molten end after the zone levelling was finished and then the zone heater was passed down the ingot for the last time. This method was not successful in growing large crystals. However, it was found that adjusting the ingot thickness allowed quite large single crystals to be grown with the zone heater. This effect is due to the heat flow in the ingot itself. If the temperature gradients are suitable, certain crystals will dominate the growth, even if several crystals start to grow at the beginning. The other crystals are forced to grow out towards the edges of the ingot and stop growing altogether after a time. Several single crystal bars about 4 in. long and 3/8 in. diameter were grown in this way. This type of growth also suppressed the lineage problem.

It was necessary to anneal the alloys after zone levelling to further homogenize the tin concentration. Each alloy was annealled at 600°C for about one week. The annealling time was judged in the following way. Several dHvA measurements were made with different samples and annealling times. It was found that unannealled samples of the same concentration showed less change of dHvA frequency from a pure antimony reference frequency than did those annealled for a time. A comparison of the dHvA frequencies of samples annealled one, then two weeks indicated no significant change. All the samples used for measurements were therefore annealled for ∿ 1 week at 600°C. Again, a helium atmosphere was used to reduce the vaporization loss of antimony.

A small single crystal sample suitable for the dHvA apparatus was spark cut out of an ingot. The presence of the prominent trigonal cleavage plane and the binary slip lines on its surface made rough orientation of each crystal rather easy. The samples were cubes of about 2 mm per side cut nearly along the binary and bisectrix axes. These crystals were mounted on a glass rod with water-soluble cement and oriented by back reflection Laue photographs so the appropriate axis (binary or bisectrix) was aligned horizontally. The crystal was then inserted into the sample holder while still mounted on the glass rod and glued into place with Glyptal cement. After the cement had dried, the glass rod was removed and the sample was ready for experiments. The transfer was done on a special device designed to preserve the orientation found from the X-ray photographs. The accuracy of orientation of the crystals as estimated from the degeneracy of the dHvA frequency branches was better than 1/2 degree.

Two methods were tried in analysing the alloys for their tin content. First, an X-ray microprobe was used. This machine detects the X-rays given off when a sample is excited by bombardment with a high energy electron beam. The ratio of the X-ray intensity of an element in a sample to that of a known concentration of the element gives (after a few correction factors) the proportion of the element in the sample. A useful feature of this machine is its ability to analyse in regions of about one cubic micron, thus showing up concentration differences on a very small scale. Unfortunately, for the low concentrations used in our alloys, the accuracy was very poor.

The second method used atomic absorption analysis. If the light of a discharge tube made from the element to be detected is shone on a gas containing that element, some of the light will be absorbed because of the excitation of the element in the flame. A spectrometer selects certain wavelengths for study. An element is put into gaseous form by atomizing a liquid solution containing the element with a gas burner. The absorption is measured with respect to changes caused by a known concentration. For tin, about 100 μg/ml concentration in liquid solution gives good sensitivity. The main problem with our alloys is the difficulty of dissolving the large excess of antimony (∿ 99.7%) present while still preserving a suitably high concentration of tin. The usual solution for dissolving antimony is concentrated HCl with some HNO_3 added (aqua regia). Powdering the alloy in a steel tube makes solution easier. The solution cannot be concentrated safely by evaporation because of the volatile nature of tin chlorides. It was found that one gram of alloy dissolves in about 10 ml of acid, giving a reasonable concentration of tin but limiting the total quantity of solution to 10 to 20 ml. This amount was sufficient. The concentrations found, along with the nominal concentrations are shown in Table II. All the concentrations are lower than expected

Table II

Alloy #	nominal conc wt.%	Atomic abs conc wt.%	Atomic abs conc at.%
1	.10	.034	.035± 11%
2	.23	.17	.17 ± 5%
3	.36	.22	.23 ± 1.5%
4	.46	.23	.24 ± 1%
5	.65	.41	.42 ± 1%
6	.80	.50	.51 ± 1%
7	.50	.28	.29 ± 1%

according to the nominal concentration of tin.

CHAPTER VI

EXPERIMENTAL RESULTS

The dHvA measurements were made in the trigonal-bisectrix and trigonal-binary planes. The trigonal-bisectrix plane contains a maximum and the minimum principal branch frequency while the trigonal-binary plane contains the other principal branch maximum. These three extremal frequencies give the basic shape of each Fermi surface pocket.

Figures 4 to 9 show the dHvA frequencies as a function of angle for six samples in the two planes. Samples with concentrations greater than .28 wt.% tin did not show any dHvA effect. Table III lists the maximum and minimum frequencies for the principal branches. The harmonic and sum frequencies found in the Fourier analysis have been removed from the figures. The six hole pieces are always twofold degenerate so only three hole branches at most appear. All three occur in the trigonal-binary plane while only two appear in the trigonal-bisectrix plane. The splitting of the degeneracy in this plane which is caused by slight misorientation of a crystal is a good indicator of the accuracy of crystal alignment. The degeneracy of the three electron pockets behaves in the same way. The data are fairly complete for the hole surface, except at the highest concentration but the higher frequency parts of the electron surface could not be detected in our experiments.

Figure 4 dHvA frequencies of pure antimony in the trigonal-binary and trigonal-bisectrix planes.

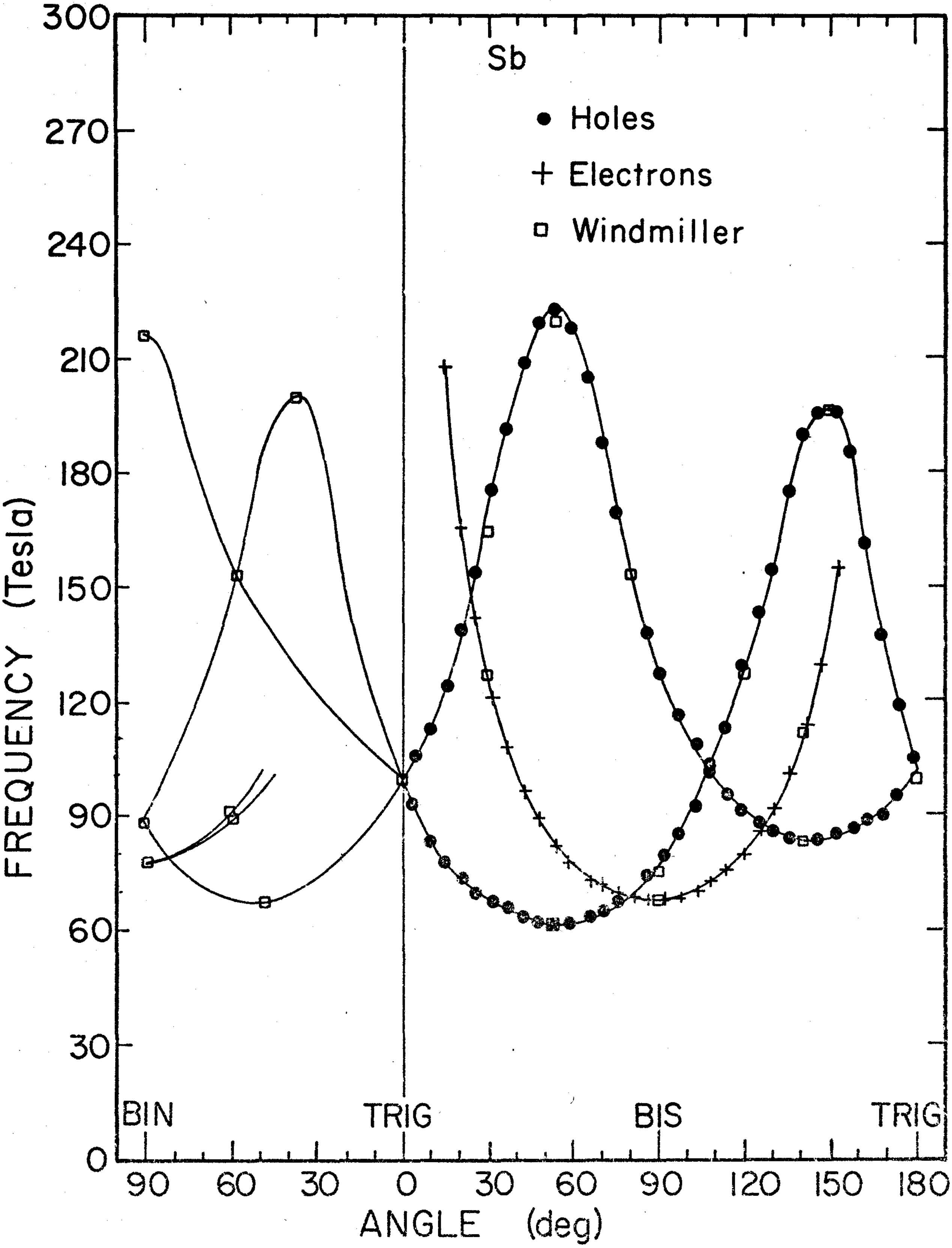
Sb
● Holes
+ Electrons
□ Windmiller
FREQUENCY (Tesla)
0
30
60
90
120
150
180
210
240
270
300
BIN
TRIG
BIS
TRIG
90
60
30
0
30
60
90
120
150
180
ANGLE (deg)

Figure 5 dHvA frequencies of antimony with 0.034 wt% tin in the trigonal-binary and trigonal-bisectrix planes.

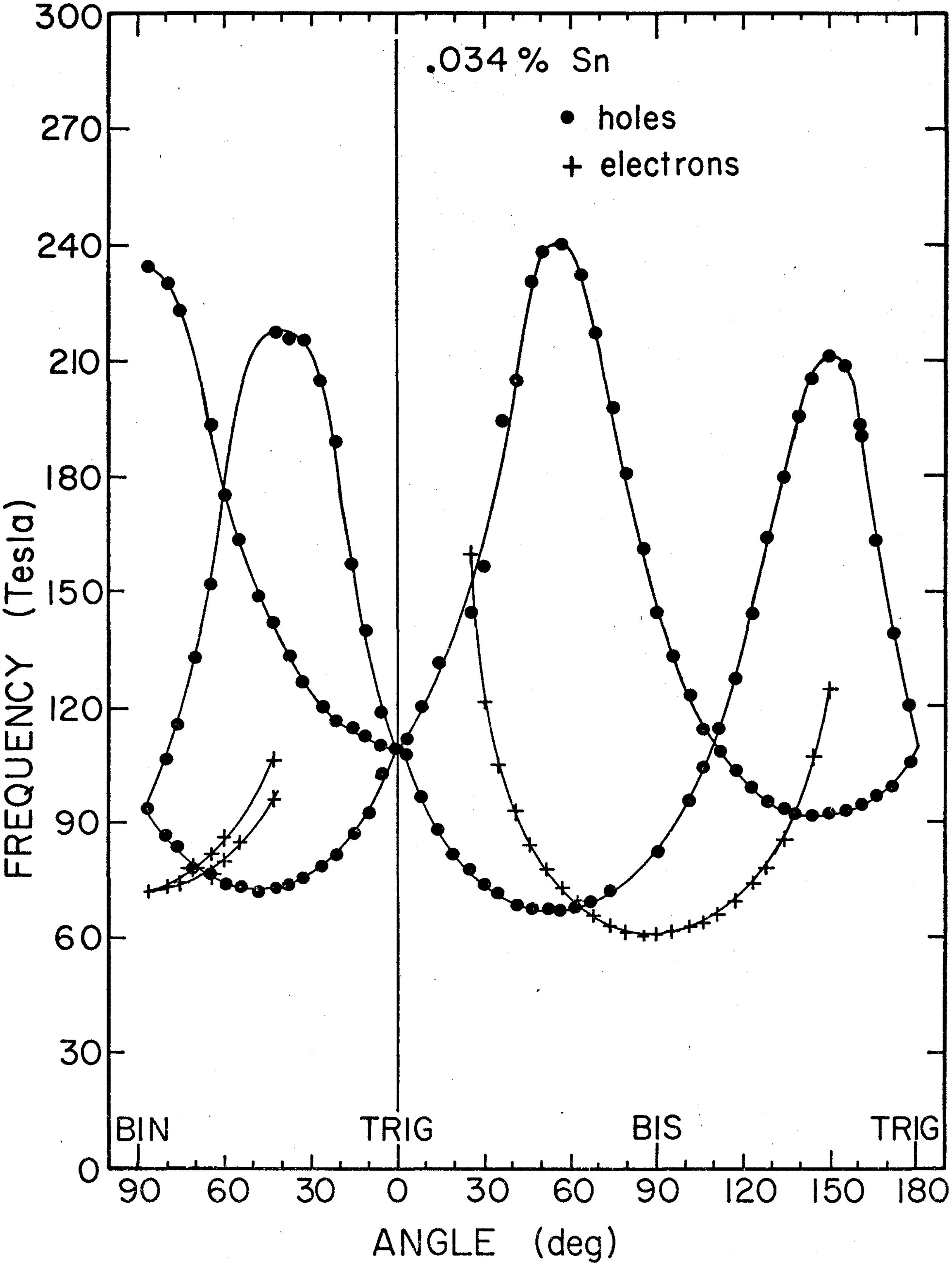
.034 % Sn
● holes
+ electrons
FREQUENCY (Tesla)
300
270
240
210
180
150
120
90
60
30
0
BIN
TRIG
BIS
TRIG
90
60
30
0
30
60
90
120
150
180
ANGLE (deg)

Figure 6 dHvA frequencies of antimony with 0.17 wt% tin in the trigonal-binary and trigonal-bisectrix planes.

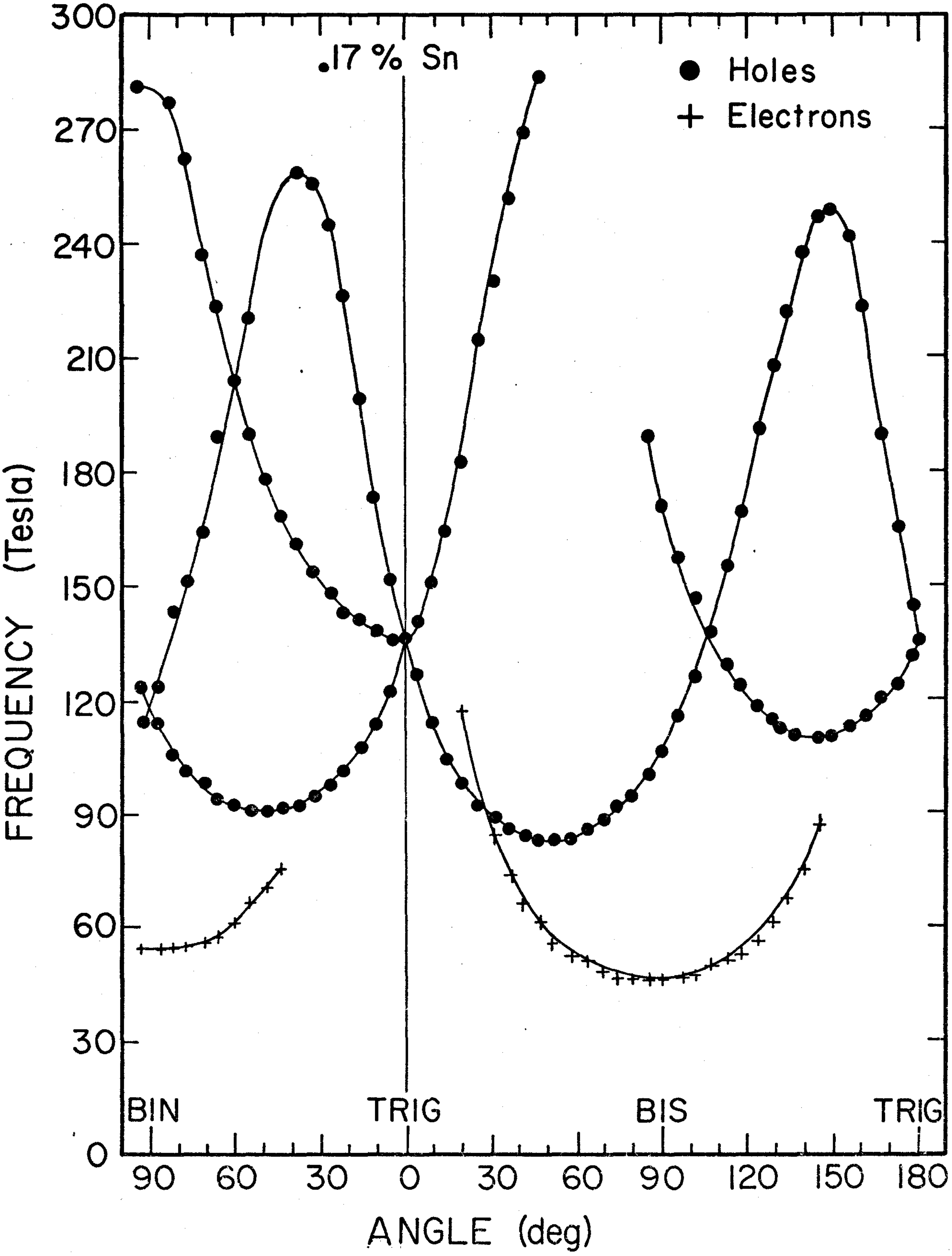
.17 % Sn
● Holes
+ Electrons
FREQUENCY (Tesla)
300
270
240
210
180
150
120
90
60
30
0
BIN
TRIG
BIS
TRIG
90
60
30
0
30
60
90
120
150
180
ANGLE (deg)

Figure 7 dHvA frequencies of antimony with 0.22 wt% tin in the trigonal-binary and trigonal-bisectrix planes.

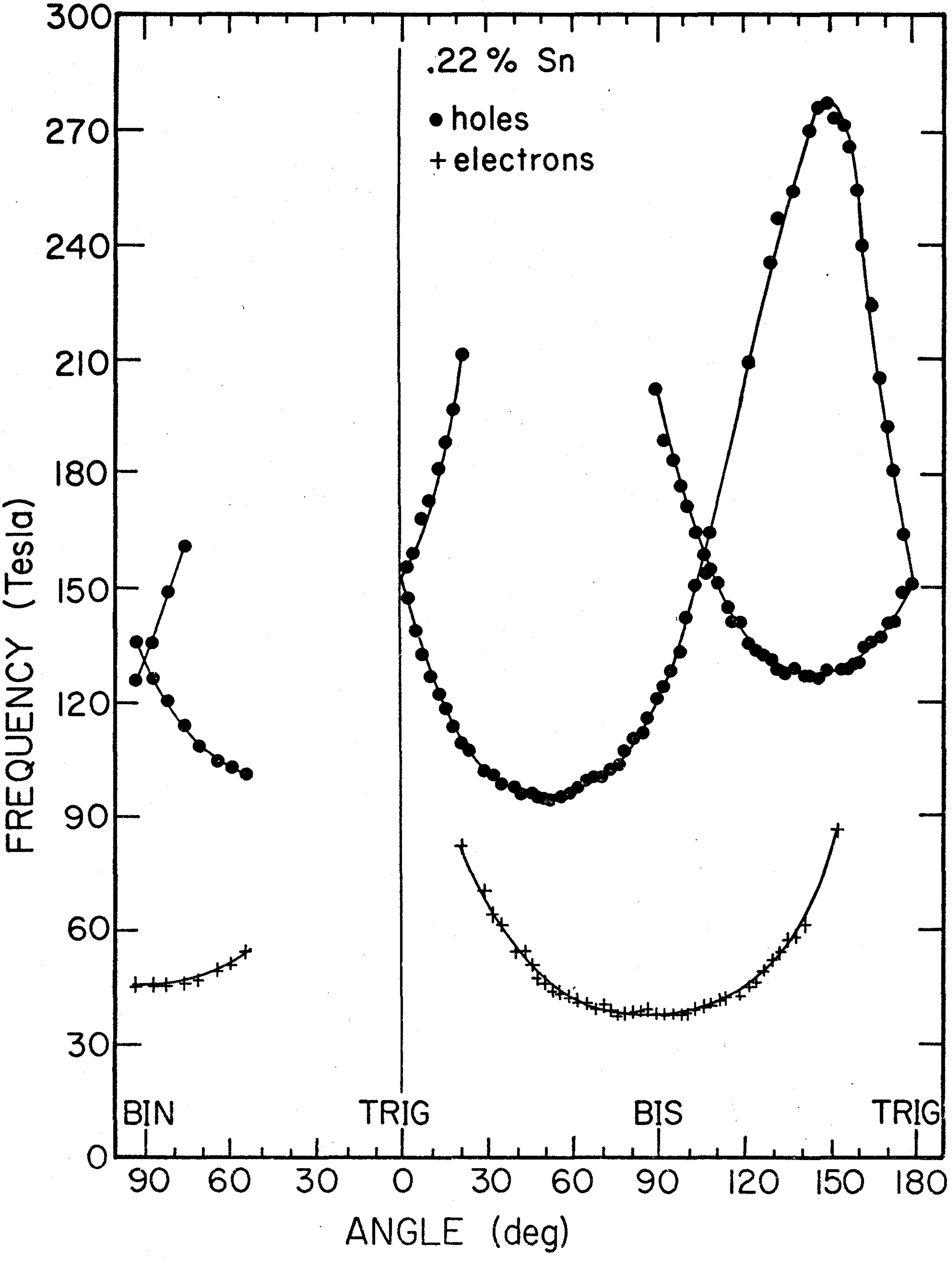
.22 % Sn
● holes
+ electrons
FREQUENCY (Tesla)
300
270
240
210
180
150
120
90
60
30
0
BIN
TRIG
BIS
TRIG
90
60
30
0
30
60
90
120
150
180
ANGLE (deg)

Figure 8 dHvA frequencies of antimony with 0.23 wt% tin in the trigonal-binary and trigonal-bisectrix planes.

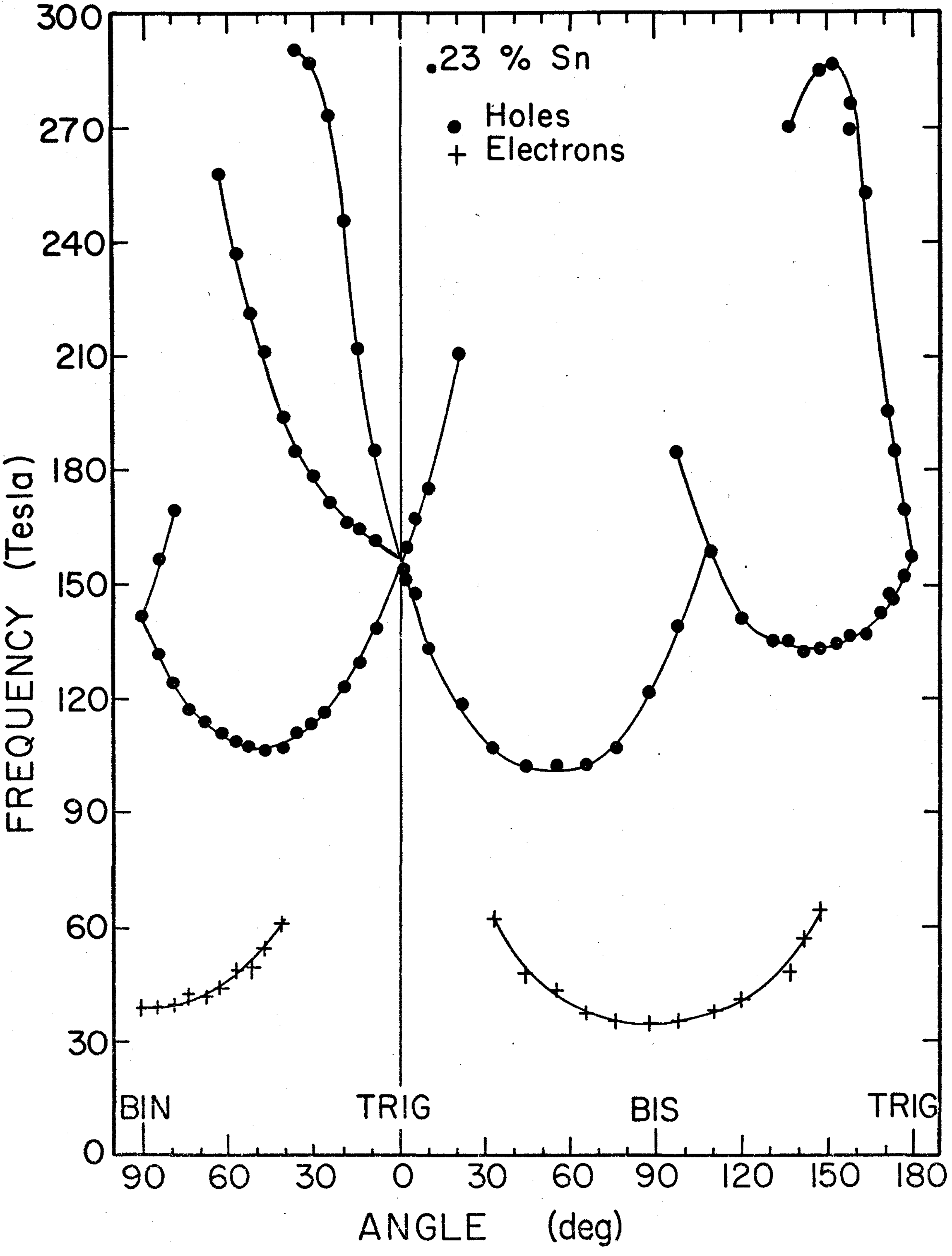
.23 % Sn
● Holes
+ Electrons
FREQUENCY (Tesla)
300
270
240
210
180
150
120
90
60
30
0
BIN
TRIG
BIS
TRIG
90
60
30
0
30
60
90
120
150
180
ANGLE (deg)

([illegible] page [illegible])

Figure 9 dHvA frequencies of antimony with 0.28 wt% tin in the trigonal-bisectrix plane.

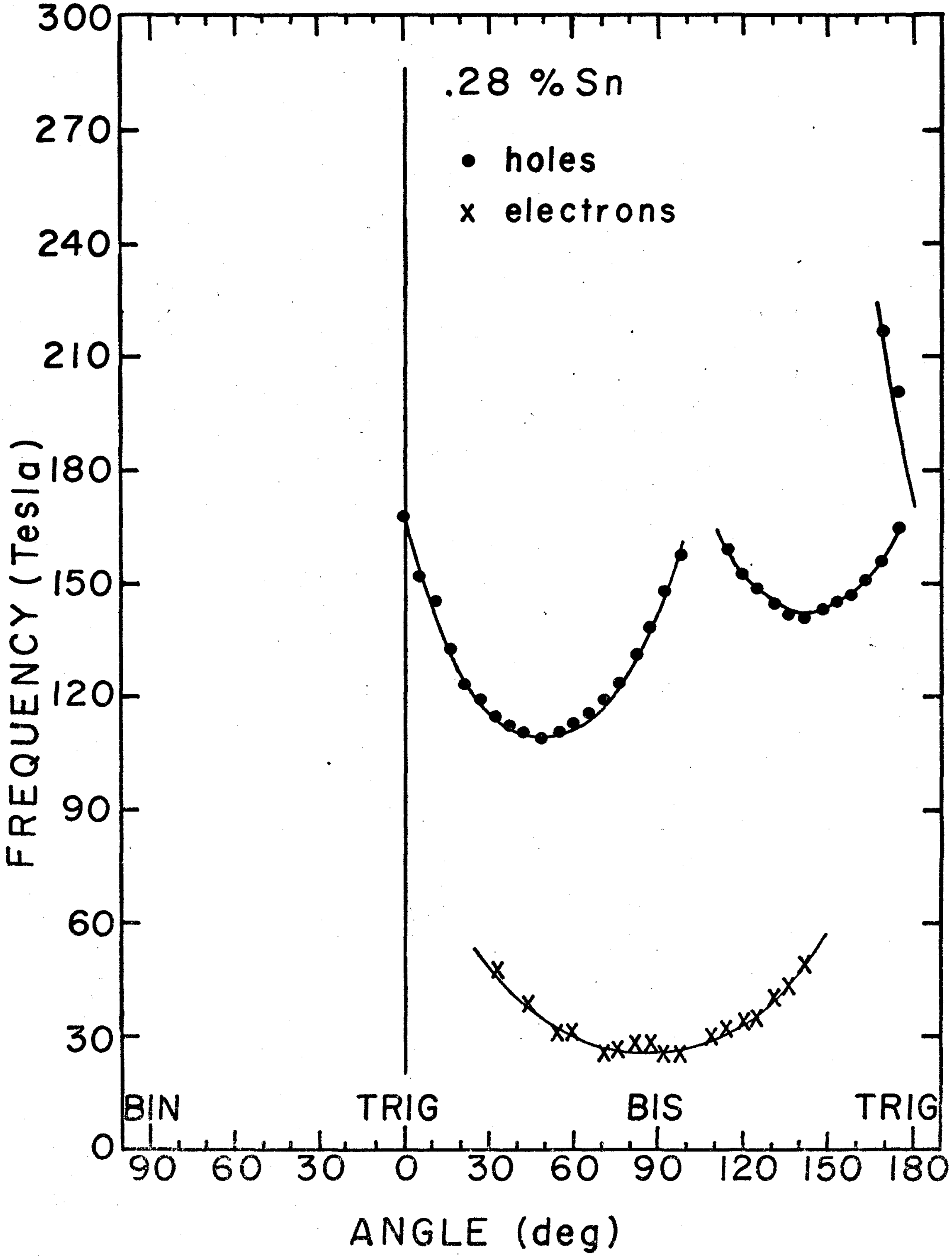
.28 % Sn
● holes
x electrons
FREQUENCY (Tesla)
ANGLE (deg)
300
270
240
210
180
150
120
90
60
30
0
BIN
TRIG
BIS
TRIG
90
60
30
0
30
60
90
120
150
180

TABLE III

dHvA frequencies, cyclotron masses and Dingle temperatures in Sb and Sb alloys

			Trigonal Bisectrix					Trigonal-Binary
conc. at.%	el. freq. min. (T)	$(\frac{m_e^*}{m})$	$(T_D)_e$ (°K)	hole freq. min. (T)	$\frac{m_h^*}{m}$	$(T_D)_h$ (°K)	hole freq. max. (T)	hole freq. max. (T)
0.00	68	0.080	2.9	61.5	0.063	2.5	197	216
0.035	61	0.078	4.5	67.0	0.064	3.3	211	234
0.017	46.5	0.063	7.6	83	0.072	6.2	249	281
0.23	38	0.058	-	95	0.078	-	271	-
0.24	34	0.057	8.5	101	0.076	11.5	287	-
0.29	26	0.054	-	109	0.085	-	-	-

The overall quality of the data decreases as the concentration increased, since alloying raises the Dingle temperature (Table III). Figures 10 and 11 show the principal hole and electron branches respectively for the different concentrations. Notice that the hole frequencies increase and electron frequencies decrease as tin atoms are added. Figure 12 shows the increase and decrease of the four extremal frequencies versus concentration. The frequencies found in pure antimony are in good agreement with the values of Windmiller (1966).

The maximum and minimum frequencies in the trigonal-bisectrix plane are 90° apart if the Fermi surface is an ellipsoid. The data indicate there is a 5° deviation from 90° for the hole surface. There is not sufficient information to determine the deviation for the electrons. The angle of deviation remains constant with alloying as does the angular position of the maximum and minimum frequencies with respect to the trigonal axis.

The frequencies were obtained from the original data by Fourier analysis. The basic program relied on the Fast Fourier Transform (FFT) algorithm, an efficient way of computing the Fourier coefficients of equally spaced, digitized data. Subsidiary programs were used for magnetic tape decoding and preparatory analysis of the data.

The cyclotron masses were found at the principal electron and hole minima in the trigonal-bisectrix plane

Figure 10 Principal hole dHvA frequencies compared as a function of concentration.

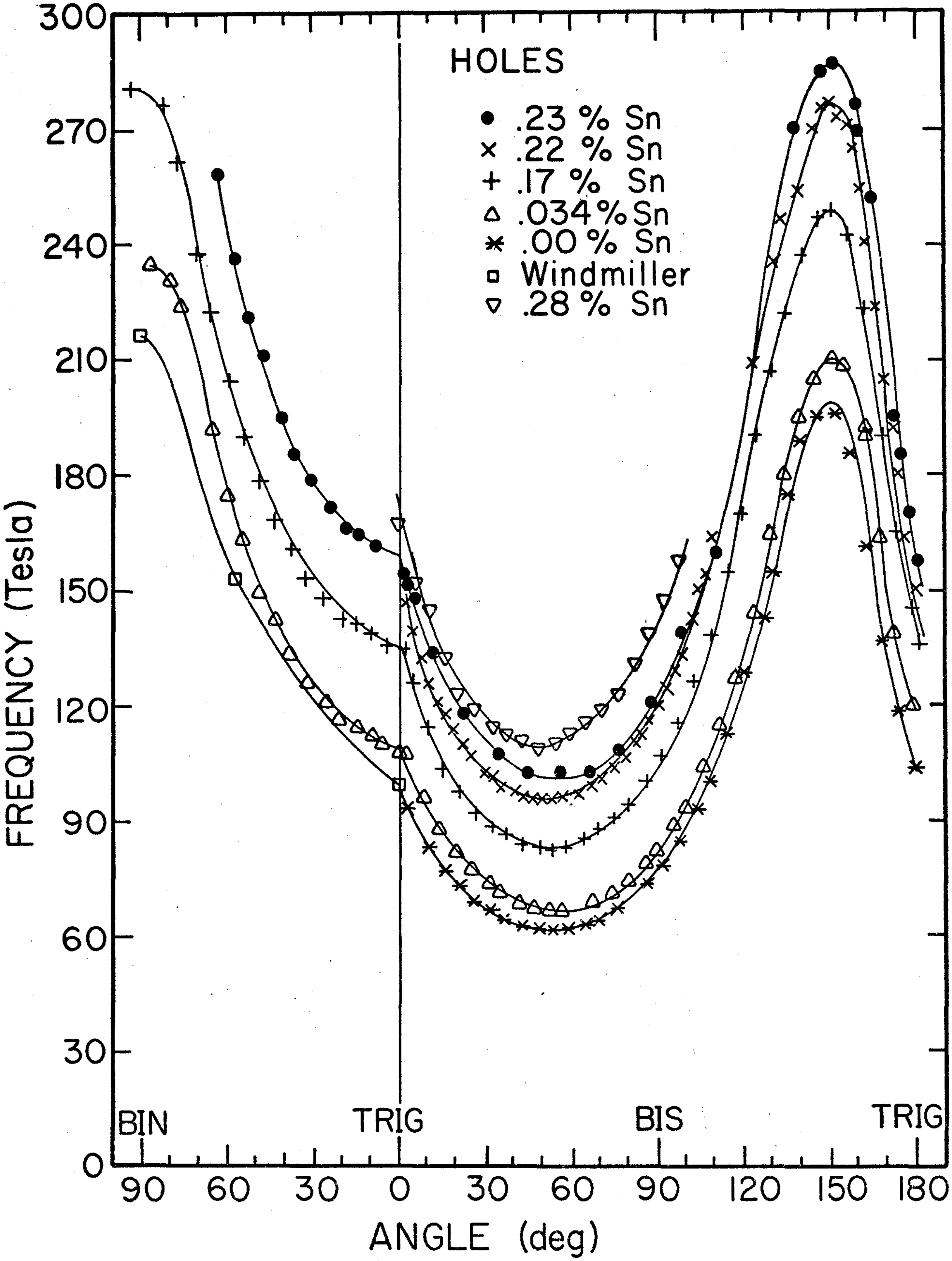
HOLES
● .23 % Sn
× .22 % Sn
+ .17 % Sn
△ .034 % Sn
✳ .00 % Sn
□ Windmiller
▽ .28 % Sn
FREQUENCY (Tesla)
300
270
240
210
180
150
120
90
60
30
0
BIN
TRIG
BIS
TRIG
90
60
30
0
30
60
90
120
150
180
ANGLE (deg)

Figure 11 Principal electron dHvA frequencies compared as a function of concentration.

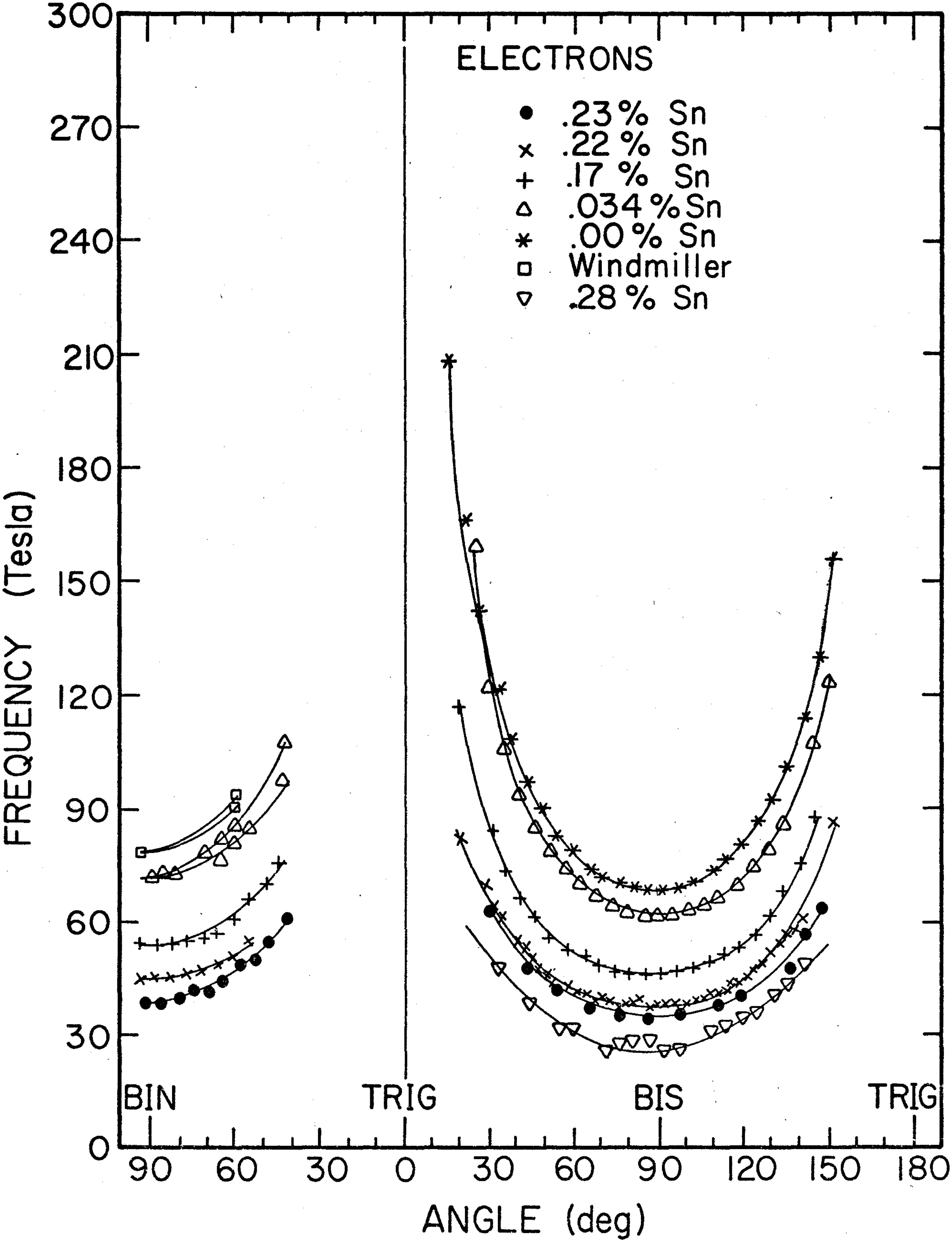
ELECTRONS
● .23 % Sn
× .22 % Sn
+ .17 % Sn
△ .034 % Sn
✱ .00 % Sn
□ Windmiller
▽ .28 % Sn
FREQUENCY (Tesla)
0
30
60
90
120
150
180
210
240
270
300
ANGLE (deg)
90
60
30
0
30
60
90
120
150
180
BIN
TRIG
BIS
TRIG

Figure 12 Extremal frequencies for electrons and holes versus concentration.

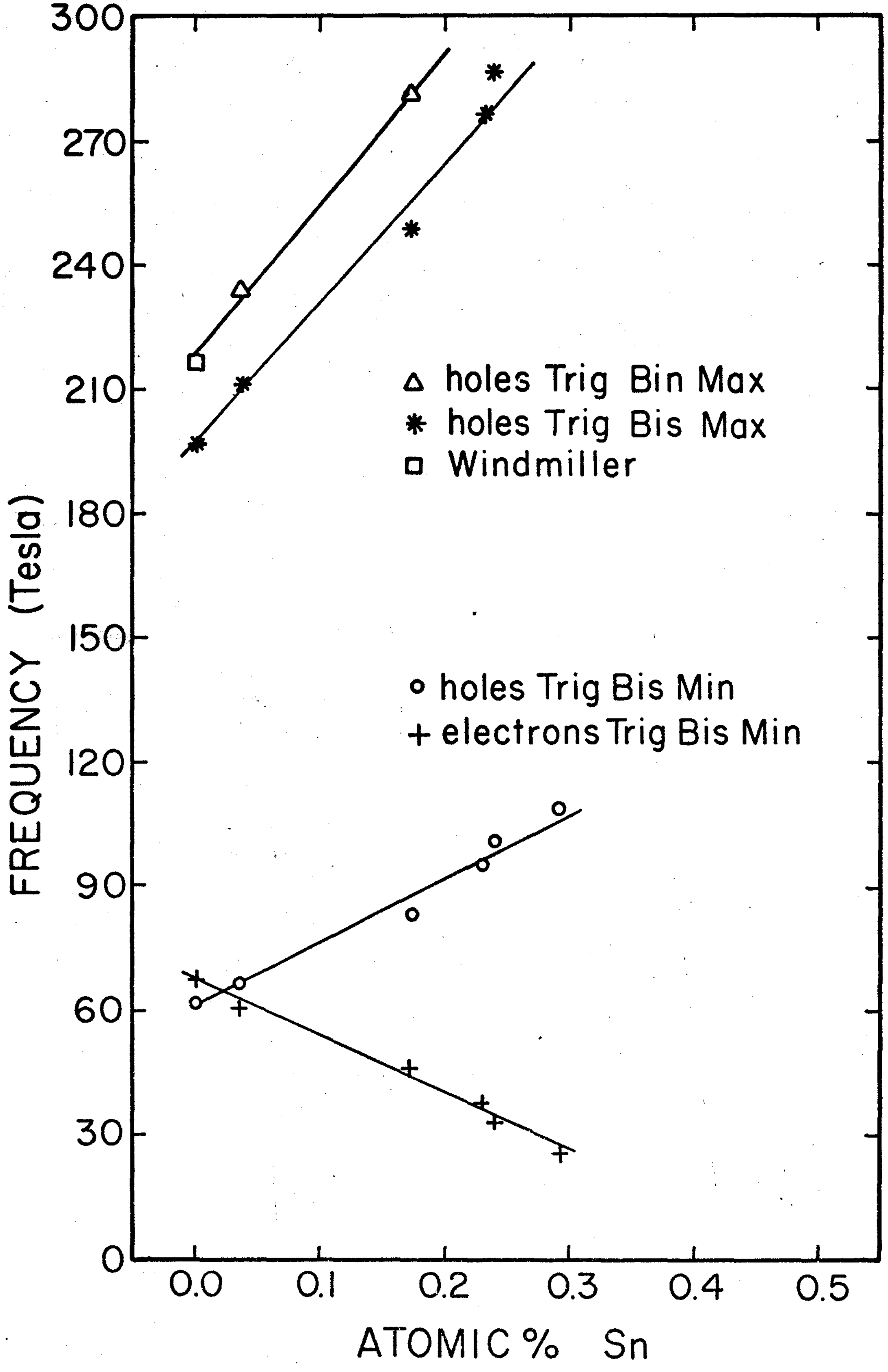

300
270
240
210
180
150
120
90
60
30
0
FREQUENCY (Tesla)
0.0
0.1
0.2
0.3
0.4
0.5
ATOMIC % Sn
△ holes Trig Bin Max
✱ holes Trig Bis Max
□ Windmiller
○ holes Trig Bis Min
+ electrons Trig Bis Min

from the temperature dependence of the dHvA amplitude at constant field. If the mass is large, the mass is found by plotting the natural logarithm of the ratio of amplitude to temperature against temperature for the frequency of interest. This gives a straight line, whose slope is proportional to the mass and inversly proportional to the field. The constant does not have any significance, being a complicated function of unknown quantities. Unfortunately this simple expression only applies if the approximation $\sinh(x) \sim e^{x}/2$ can be made. This is true if $x \geq 3$ with an error of <.25%. Since

$$x = \frac{14.69\ m^{*}\ T}{H}$$

where H is in tesla, T in degrees Kelvin and m^{*} in free electron masses, the smallest value of x that occurs in the present apparatus is $x \sim 3\ m^{*}$ if the minimum temperature of ∿1°K and maximum field of ∿5T are used. If $m^{*} > 1.$ the above approximation is reasonable. Antimony and its alloys have $m^{*} \leq .1$ so the full expression for the dHvA amplitude must be used. From Eq. (1) and (14), the amplitude is ($\alpha = \frac{2\pi^{2}k_{B}}{e\hbar} = 14.69$ Tesla/°K)

$$y(T) = \frac{f(m^{*})\,T e^{-\alpha m^{*} T_{D}/H}\ J_{2}(2\pi f h/H^{2})}{H^{1/2}\ \sinh(\alpha m^{*}T/H)} \tag{15}$$

A more convenient form results if Eq. (15) is normalized by dividing through by $y(T_{o})$ at constant H. This gives

$$\frac{y(T)}{y_{o}(T_{o})} = \frac{T\ \sinh(\alpha m^{*}T_{o}/H)}{T_{o}\ \sinh(\alpha m^{*}T/H)}\ . \tag{16}$$

This is a function of one unknown, m*, and can be solved in two ways.

The first makes use of the fact that $\sinh(x) = e^x/2\,(1-e^{-2x})$ so the term $1-e^{-2x}$ can be treated as a correction factor. The slope of $\ln(\frac{y\,T_o}{y_o T})$ vs. $T_o - T$ is used to find a first estimate of the mass. With this estimate, the correction factor

$$\ln\left(\frac{1-e^{-2\alpha m^* T/H}}{1-e^{-2\alpha m^* T_o/H}}\right)$$

is applied and a second estimate of the mass is made. This process is repeated several times until the value of mass converges. It is obvious that this procedure is an extension of the method for finding large masses mentioned previously.

The second method is more direct since it minimizes the least squares expression

$$\sum_i \left(\frac{y_i T_o}{y_o T_i} - \frac{\sinh(\alpha m^* T_o/H)}{\sinh(\alpha m T_i/H)}\right)^2 .$$

One variable minimizations of this type are easily done numerically, for instance by the golden section alogrithm. The results are nearly identical to those of the previous method. The directness and speed of the minimization procedure probably make it the better choice.

The main difficulty that occurs when calculating the cyclotron mass is separating the effects of the different dHvA frequencies. If there are only two frequencies present which beat together, it is possible to separate the two components fairly easily (Everett 1970). If the frequency separation is large, electronic filtering will remove or suppress the unwanted frequencies. However, in many cases, there are two or more similar frequencies of comparable amplitude. A Fourier transform can separate the different frequencies and allow each frequency peak to be isolated. The peaks are not delta functions, but have some frequency width associated with them. This width contains information on the envelope function of the particular dHvA frequency. Eq. (15) describes the envelope function of a single dHvA frequency. For simplicity, consider the case of Fig.13 with two dHvA components F_1 and F_2. Suppose the cyclotron mass of F_1 is required (F_1 is lower frequency). To remove the effects of F_2, the components not associated with F_1 are set to zero (Fig.13b). The isolation must be done with the Fourier transform sine and cosine coefficients rather than the amplitude as suggested in Fig. 13. The sine and cosine coefficients of F_1 are used in an inverse Fourier transform to restore the field dependence of F_1 alone. Then one of the previously discussed methods of finding the cyclotron mass is applied.

Two related problems occur with the inverse Fourier transform. If the F_1 and F_2 widths are large and F_2-F_1 is small, then the overlap of the two peaks will have made the individual Fourier components inaccurate in this region,

Figure 13a Typical Fourier peaks before frequency separation.

Figure 13b Separated Fourier peak. Dashed lines are an approximation to the truncated tails of the peak.

Figure 13c Cyclotron mass for pure antimony as a function of reciprocal field.

Figure 13d Cyclotron mass for .23 wt% Sn alloy as a function of reciprocal field.

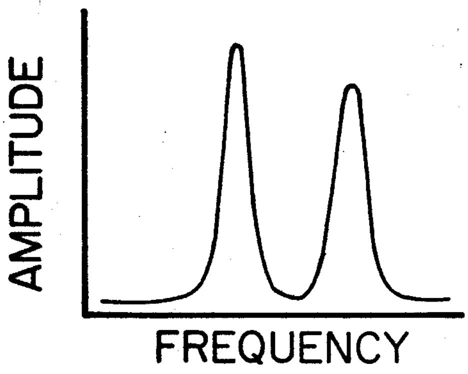
AMPLITUDE
FREQUENCY

(a)

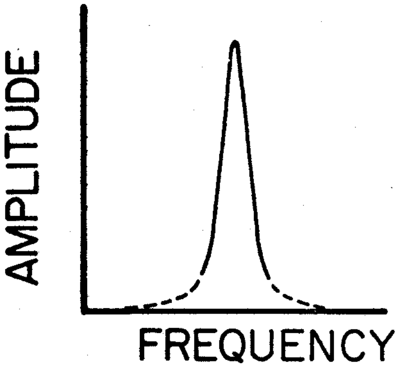
AMPLITUDE
FREQUENCY

(b)

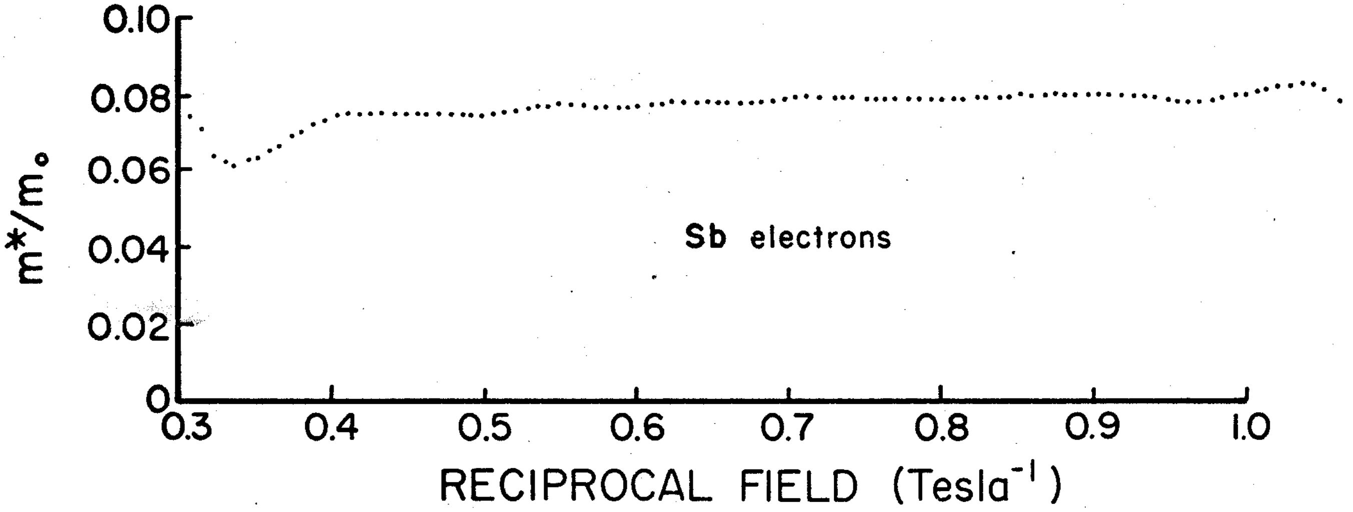
m*/m₀
0.10
0.08
0.06
0.04
0.02
0
0.3
0.4
0.5
0.6
0.7
0.8
0.9
1.0
Sb electrons
RECIPROCAL FIELD (Tesla⁻¹)

(c)

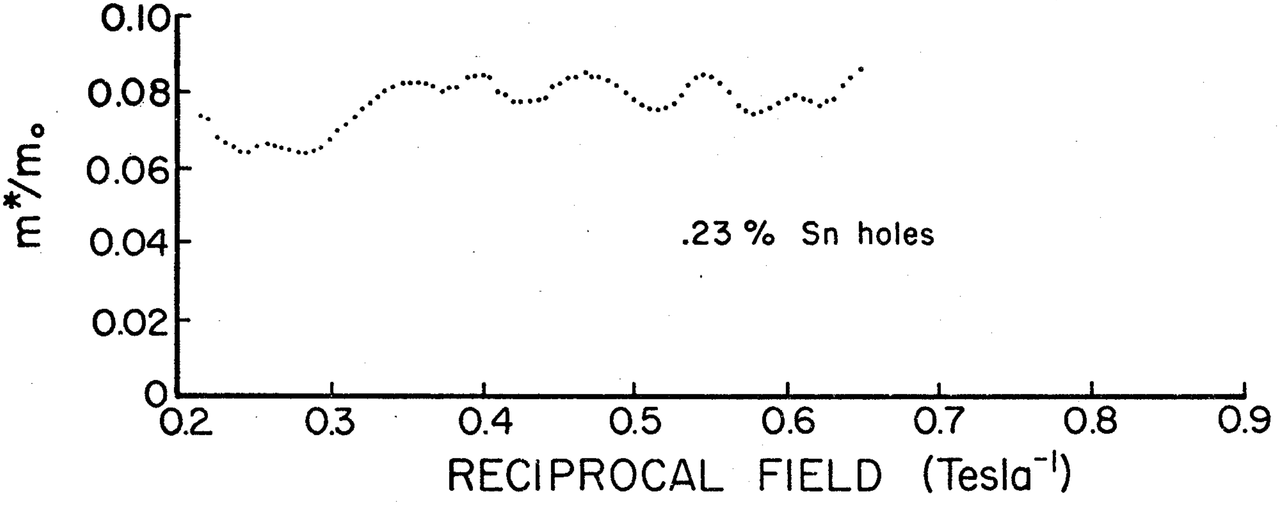
m*/m₀
0.10
0.08
0.06
0.04
0.02
0
0.2
0.3
0.4
0.5
0.6
0.7
0.8
0.9
.23 % Sn holes
RECIPROCAL FIELD (Tesla⁻¹)

(d)

so the inverse Fourier transform will also be inaccurate. For our alloys, this was not a serious problem since the frequencies were always well separated compared with the peak width. Also, there is in general a background present in the Fourier analysis. When F_1 is isolated, there is a step at each end of the passband caused by the background and perhaps a slight frequency overlap with F_2. When the inverse Fourier transform is done, these steps generate deviations in the amplitude at the upper and lower fields. These deviations can be suppressed by approximating the missing tails of peak F_1 to a function $A/|F-F_1|$ which removes the discontinuity in function value (Fig. 13b). A discontinuity in the slope will remain.

The cyclotron mass can now be found as a function of field. Two results from our analysis are shown in Fig. 13c and d. The upper and lower ends show variation caused by residual discontinuities. An average over the central region gives the value of the cyclotron mass. Fig. 13c shows the good results obtained when there is a large signal to noise ratio and high frequency resolution resulting from a pure sample. Fig. 13d shows similar results in an alloy where the signal quality and frequency resolution was poorer because of the higher Dingle temperature. This system of analysing the cyclotron mass allows us to avoid the problems of field dependent variations (Everett 1970) and enables us to average over field. The cyclotron mass values presented in Table III and shown in

Fig. 14 are the averages obtained in this way except for the .29 at% sample. The electron and hole masses at this concentration were determined from 10 and 12 oscillations. on a strip chart recorder without any Fourier analysis. Notice that there is a significant change with concentration for both holes and electrons. The values obtained in antimony are a few percent lower than those found by Windmiller (1966).

The Dingle temperature is related to the field variation of the amplitude at constant temperature. After the cyclotron mass has been found, the Dingle temperature is calculated from the slope of

$$\ln\left(\frac{Y}{Y_o}\,\frac{\sqrt{H}}{\sqrt{H_o}}\,\frac{\sinh(\alpha m^*T/H)}{\sinh(\alpha m^*T/H_o)}\,\frac{J_2(\lambda_o)}{J_2(\lambda)}\right)$$

vs. reciprocal field difference $1/H - 1/H_o$. The same frequency separation method used for the cyclotron mass was also used here to separate different dHvA components. The values of Dingle temperature are shown in Table III. The Dingle temperature increases roughly linearly with concentration.

The number of carriers present in the metal is directly proportional to the volume of the Fermi surface. The volume is easily calculated if the Fermi surface is approximated by an ellipsoid since, in that case,

$$V = \frac{4\pi}{3}\left(\frac{2e}{\hbar}\right)^{3/2}(F_1F_2F_3)^{1/2}$$

where F_1, F_2 and F_3 are the three extremal frequencies. It is shown by Aurbach et al. (1971) by using an eighth order spherical harmonic approximation to the antimony electron

Figure 14 Cyclotron mass of hole and electron minima in the trigonal-bisectrix plane versus concentration.

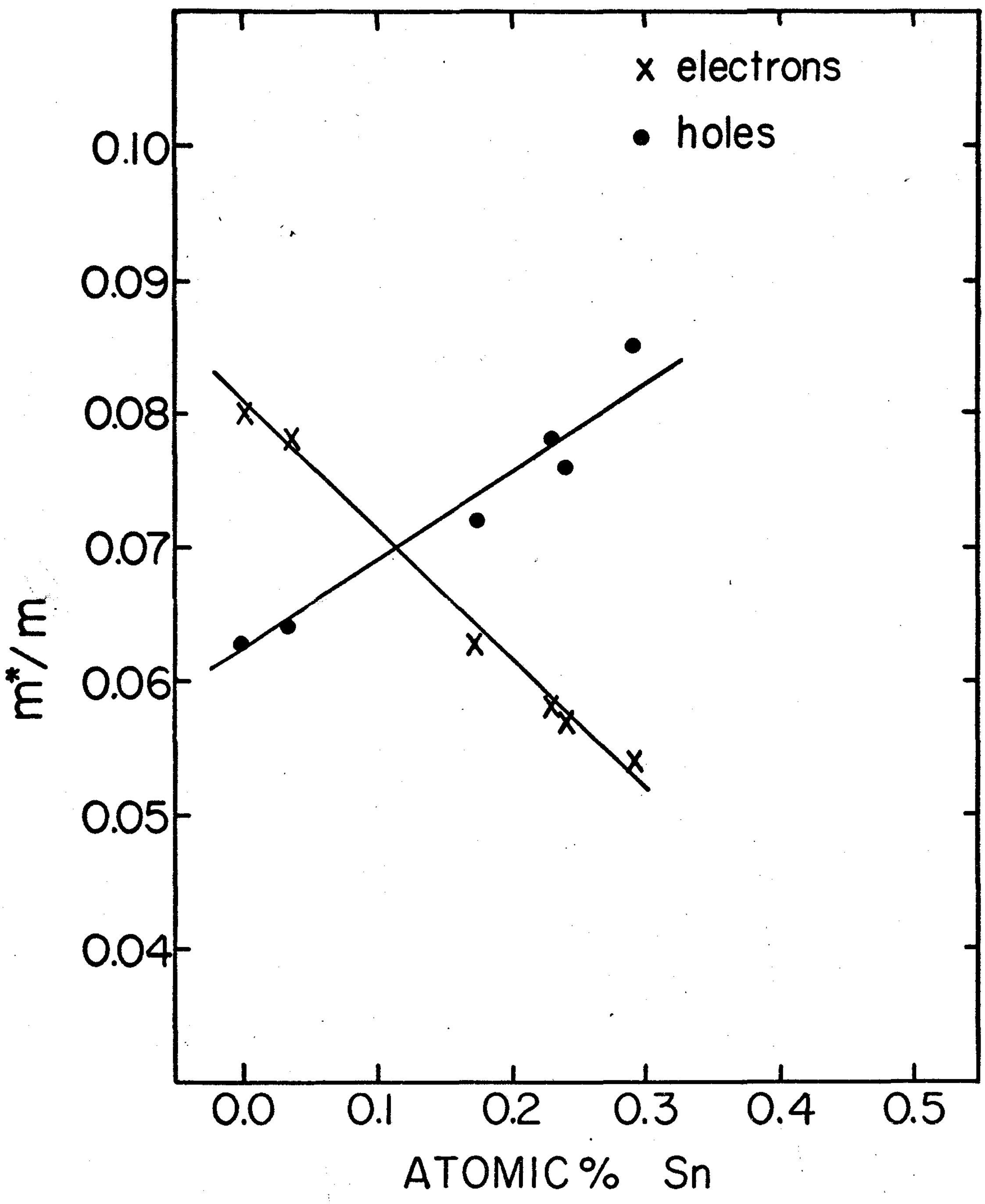
x electrons
● holes
m*/m
0.10
0.09
0.08
0.07
0.06
0.05
0.04
0.0
0.1
0.2
0.3
0.4
0.5
ATOMIC % Sn

surface that the number of carriers as deduced from the Fermi surface volume is $5.543 \times 10^{19}/\mathrm{cm}^3$. A calculation (Windmiller 1966) using the ellipsoidal approximation gave $5.54 \times 10^{19}/\mathrm{cm}^3$. Since the electron surface is bent ∿4° from an ellipsoid and the hole surface is bent ∿6°, it appears that the ellipsoidal approximation is quite adequate for calculating the volumes of the hole Fermi surface.

For the electron pocket, there is no information on the maximum frequencies except in pure antimony. Therefore it is necessary to estimate the volume by assuming that the relative lengths of the major and minor axes remain the same in the alloys. If P is defined as the ratio of the alloy minimum frequency to the antimony minimum frequency, then the volume of the alloy Fermi surface is

$$V(\mathrm{ALLOY}) = P^{3/2}\ V(\mathrm{Sb}) \quad .$$

For the holes, the data are more complete. The three highest concentration alloys lack the trigonal-binary maxima. These have been extrapolated from the three lower values to allow for a shape change with concentration. The extrapolated values are 304T, 308T and 328T. The missing trigonal bisectrix maximum (297T) for the 0.29 at% alloy has been found in the same way. A shape change of the hole surface is clearly indicated by the differences in the trigonal bisectrix maximum to minimum frequency ratios found in antimony and the alloys. This ratio gives a measure of the relative axial lengths in the ellipsoidal approximation. The ratio is 3.2

in pure antimony and declines to 2.8 for a .24 at % Sn alloy. This is a 13 percent change suggesting that the hole surface is becoming less elongated.

Table IV shows the total electron and hole carrier densities. The total allows for the three electron and six hole Fermi surface pockets. The total change of carrier density is compared with the number of tin atoms added.

TABLE IV

Carrier density in Sb and Sb(Sn) alloys and the change of density from that of pure Sb

conc. at.% Sn	# of Sn /cm^3	# of el. /cm^3	# of holes /cm^3	total change /cm^3	total change /# of Sn
0.00	0.0×10^{19}	5.55×10^{19}	5.52×10^{19}	-	-
0.035±11%	1.2×10^{19}	4.74×10^{19}	6.18×10^{19}	1.44×10^{19}	1.20
0.17 ±5%	5.7×10^{19}	3.11×10^{19}	8.19×10^{19}	5.08×10^{19}	.89
0.23 ±1.5%	7.6×10^{19}	2.08×10^{19}	9.61×10^{19}	7.53×10^{19}	.99
0.24 ±1 %	7.9×10^{19}	1.96×10^{19}	10.2×10^{19}	8.24×10^{19}	1.04
0.29 ± 1%	9.6×10^{19}	1.58×10^{19}	11.1×10^{19}	9.5×10^{19}	.99

CHAPTER VII

DISCUSSION

A. Rigid Band Model

When an atomic concentration C of impurities is added to a pure metal, the rigid band model assumes that no change of band structure will take place but that the electron concentration per atom is changed by ZC where Z is the valence difference between the host and impurity. This can be written in terms of a Fermi energy shift ΔE (Heine 1954) as

$$\Delta E = \frac{ZC}{D_o(E_F)} \tag{17}$$

where $D_o(E_F)$ is the density of states in the pure metal at the Fermi energy E_F. This expression assumes ΔE is small and $D_o(E_F)$ is not strongly energy dependent. Heine (1954) defines a parameter

$$R = \frac{A-A_o}{A_o ZC} \tag{18}$$

where $A-A_o$ is the change of Fermi surface area A from the area A_o of the pure metal. A useful expression results if A is expanded about A_o in a Taylor series in energy of the type

$$A-A_o = \left(\frac{\partial A}{\partial E}\right)_o \Delta E + \frac{1}{2}\left(\frac{\partial^2 A}{\partial E^2}\right)_o \Delta E^2 + \ldots \tag{19}$$

Putting Eq. (19) into Eq. (18) and using the definition of cyclotron mass (Eq. 1A) to provide the second derivative of A with E

$$\frac{2\pi}{\hbar^2}\left(\frac{\partial m^*}{\partial E}\right)_o = \left(\frac{\partial^2 A}{\partial E^2}\right)_o \tag{20}$$

gives

$$R = \pm \frac{2\pi\Delta E}{\hbar ZCA_o}\left(m_o{}^* + \frac{1}{2}\left(\frac{\partial m^*}{\partial E}\right)_o \Delta E\right) \quad . \qquad (21)$$

$\beta = \frac{e\hbar}{m^* c}$.

After writing

$$\left(\frac{\partial m^*}{\partial E}\right)_o = \left(\frac{\partial m^*}{\partial C}\right)_o \bigg/ \left(\frac{\partial E}{\partial C}\right)_o$$

and using Eq. (17) for ΔE, Eq. (21) becomes

$$R = \pm \frac{2\pi}{\hbar^2 A_o} \frac{m_o^*}{D_o(E_F)} \left(\frac{m_o^* + m^*(C)}{2m_o{}^*}\right) \quad . \qquad (22)$$

$m^*(C)$ is the cyclotron mass as a function of concentration as shown in Fig. 14. If the change of mass with concentration is negligible, the bracketed term in Eq. (22) becomes unity and Heine's result is obtained. The ± sign in Eq. (21) and (22) indicates whether the Fermi surface areas increase or decrease on alloying. The rigid band model can be compared with experiment by plotting $\frac{F-F_o}{F_o}$ against C. Eq.(22) can be rearranged to give

$$\frac{F-F_o}{F_o} = \frac{ZC}{\hbar eF_o D_o(E_F)} \left(\frac{m_o^* + m^*(C)}{2}\right) \quad . \qquad (23)$$

The value of $D_o(E_F)$ is 4.67×10^{-2}/atom/eV. This has been calculated from the electronic specific heat constant (McCallum and Taylor 1967 , Zebouni and Blewer 1967). A plot of Eq. (23) is presented as the dashed lines in Fig. 15 where the simple rigid band model with $m^*(C) = m_o^*$ is shown as

Figure 15 Comparison of observed frequency shifts for electrons and holes at trigonal-bisectrix minima with simple (solid lines) and mass-dependent (dashed lines) rigid-band theories.

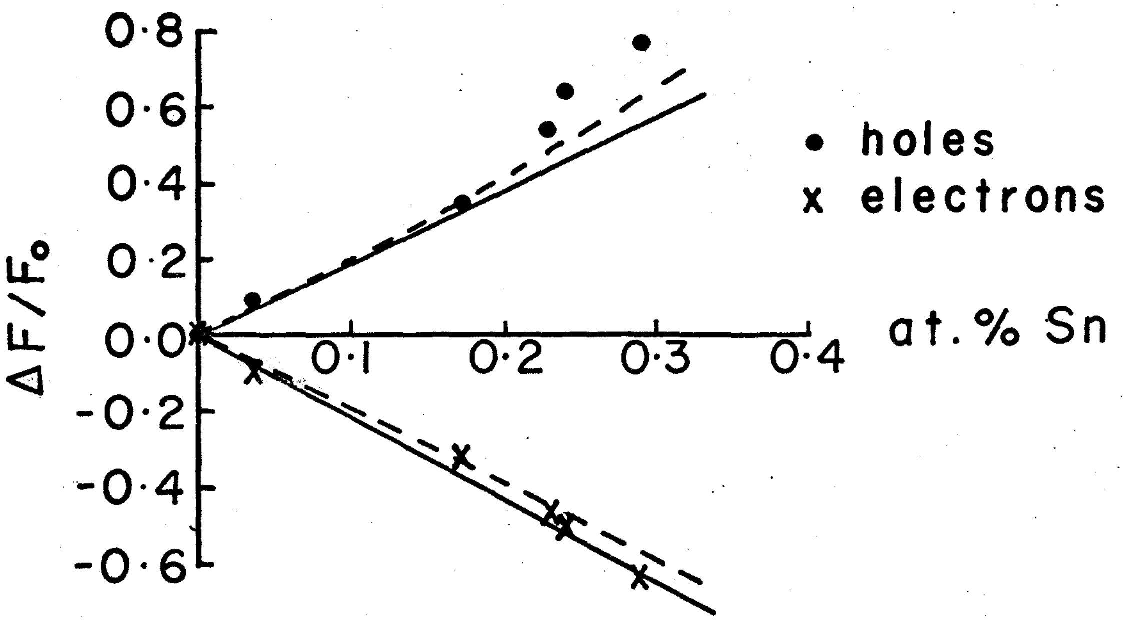
0·8
0·6
0·4
0·2
0·0
-0·2
-0·4
-0·6
ΔF/F₀
0·1
0·2
0·3
0·4
at.% Sn
● holes
x electrons

the solid lines. The agreement is quite good for the electron branch and lower concentrations of the hole branch but deviates somewhat at the two highest hole concentrations. Part of this deviation is due to the shape change found for the hole band.

The carrier concentration can be calculated from the dHvA frequencies using the ellipsoidal approximation. Table IV shows the carrier densities, total carrier density change, the number of tin atoms added and the ratio of the carrier density change to the tin density. The last column indicates that all the tin atoms are effective in changing the carrier concentration. The average value of carrier density change to tin atom density is 1.03, quite close to the rigid-band prediction of 1.00. A combination of error in the tin concentrations and the approximations made in calculating the electron volume probably accounts for the observed deviations. If the rigid-band model holds exactly, the results suggest that the electron pocket has been slightly underestimated in size, indicating that the electron axial ratio increases slightly with concentration. The fact that the number of carriers agrees quite well with the rigid-band model implies that the deviation found in Fig. 15 is caused by changes not accounted for by the simple rigid-band model. It appears that Ishizawa and Tanuma (1965) had less tin in their sample than they thought because the change in frequency is too small for their stated concentration according to our results.

Also, Epstein and Juretschke (1963) found tin removes 0.3 electrons per atom, less than that found here. No evidence of an extra set of holes as suggested by Saunders and Oktu (1968) was found. This is not too surprising since the concentrations of our alloys were considerably less. Extrapolation of our change of electron density with alloying indicates that the electron pocket will be empty at ∿0.35 at. % Sn. This is in disagreement with previous workers (Epstein and Juretschke 1963, Brown and Lane 1941) who suggested from 1 to 2 at % is required. Finally, when our results are extrapolated to the case of antimony doped with atoms of valence 6 such as tellurium, it is suggested that the hole carriers in the valence band will disappear at approximately 0.35 atomic percent.

B. Band Shapes

The three band types considered in Chapter II will be discussed: the ellipsoidal parabolic band, the ellipsoidal nonparabolic Kane (1957) band and finally a pseudopotential band.

The ellipsoidal parabolic band is described by Eq. (2) and predicts ellipsoidal Fermi surfaces and energy independent cyclotron masses. This band can be taken as a first approximation to the actual Fermi surface of antimony to describe the gross features. However, it does not predict any change of shape with concentration as observed, non-ellipsoidal behaviour or energy dependent cyclotron masses. This

E_g - C

band does enable certain calculations to be made easily, such as the carrier concentration, and will be useful later in the calculation of the energy band overlap.

The form of ellipsoidal nonparabolic band is given in Eq. (5) where when E_g is large Eq.(5) reduces to Eq.(2). In the case of antimony and its alloys, there is reason to expect E_g to be small for both the electron and hole bands (Falicov and Lin 1966). The energy surfaces are again ellipsoids but the cyclotron mass is now energy dependent. The cyclotron mass and Fermi surface area in the xy plane are given by Eq. (7) and (6). These equations can be combined to give

$$(m^*_{xy})^2 = m_o{}^2 + \frac{4}{\pi} A_{xy} \frac{m_o}{E_g} \qquad (24)$$

where $F_{xy}(= \frac{m^2 e^3}{4h^3 \varepsilon_o{}^2} A_{xy}(au))$ is the dHvA frequency in the xy plane and $m_o = (m_1 m_2)^{1/2}$. A plot of Eq. (24) using F instead of A for the electron and hole minima is shown in Fig. 16. The fitted least squares line has a negative intercept for holes and a positive intercept for electrons. The scatter of the data points makes the intercept value inaccurate. The intercept of the electron line gives $m_o/m \sim 0.012$ and hence $E_g \sim 0.06$eV. .06×10 [illegible]
The slope of the line is more accurately determined and gives a value of the $\overline{k}\cdot\overline{p}$ matrix element $E_p(=E_g/m_o)$. The matrix [illegible] element is 7.3eV for holes and 5.0eV for electrons. These values compare with 20eV for III-V semiconductors (Ehrenreich 1969)

Figure 16 Comparison of observed masses and frequencies to least squares linear fit predicted by a Kane nonparabolic band.

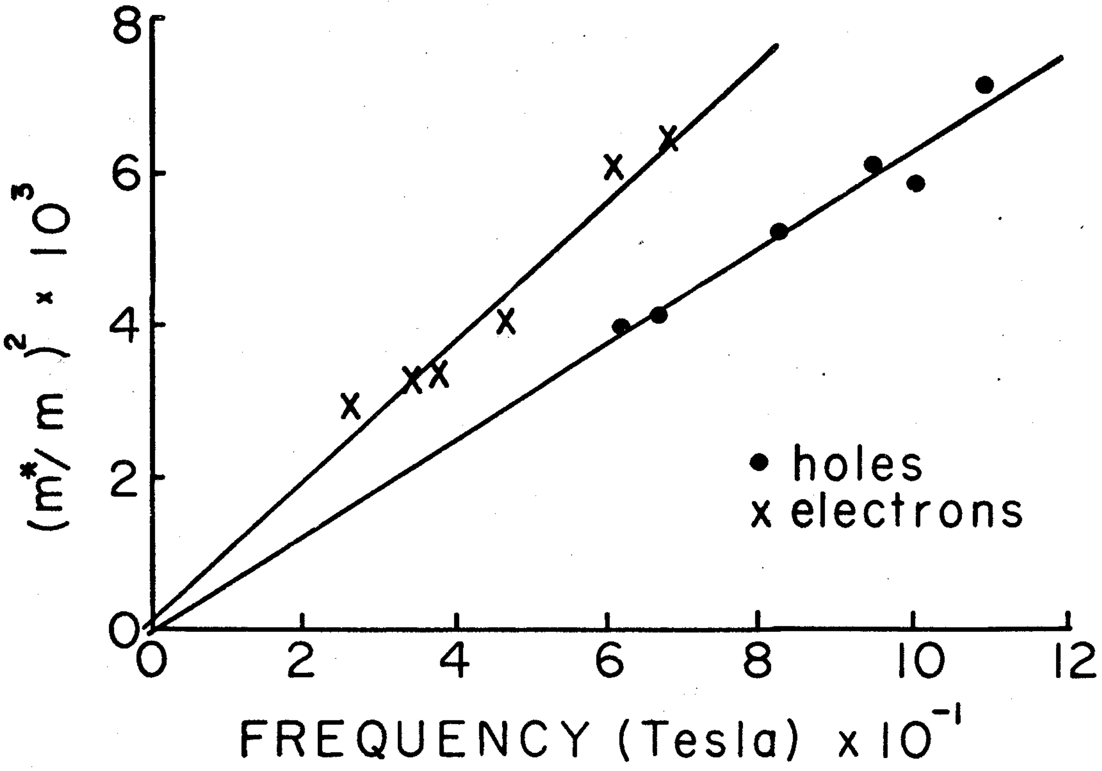

$(m^*/m)^2 \times 10^3$
8
6
4
2
0
0
2
4
6
8
10
12
FREQUENCY (Tesla) $\times 10^{-1}$
● holes
x electrons

and 8 eV for bismuth-antimony (Ellett et al. 1966). The ellipsoidal nonparabolic model describes the mass changes reasonably well and gives some insight into the band interactions, but it cannot explain the deviation from ellipticity or change of axial ratio with concentration.

The pseudopotential bands are based on the work of Falicov and Lin (1966) for pure antimony. They diagonalized an 89 by 89 determinant to find the energy bands and Fermi surfaces using a pseudopotential of the form (U in Ry., q in au)

$$U(q) = \frac{.1564\ (q^2 - 2.367)}{\exp[3.260(q^2-2.803)+1]} .$$

We have done a similar calculation using the same pseudopotential to examine the hole and electron Fermi surfaces in more detail.

A grid of points was chosen in $\bar{k}$-space around each pocket center and energy values were found for each point. Part of the grid is shown in Fig. 17 and 18. The area shown corresponds to the trigonal-binary maximum for both electrons and holes in the mirror plane. Since the electron surface has inversion symmetry only half the surface is needed. The dividing line in Fig. 18 is the Brillouin zone boundary. The axes on the planes are at an arbitrary but fixed angle from the trigonal so that each surface is described roughly in its principal coordinates. Notice that the electron minimum energy occurs at (0.0,0.0)-the L point - as it must

Figure 17 Pseudopotential hole energy grid in the trigonal-binary mirror plane.

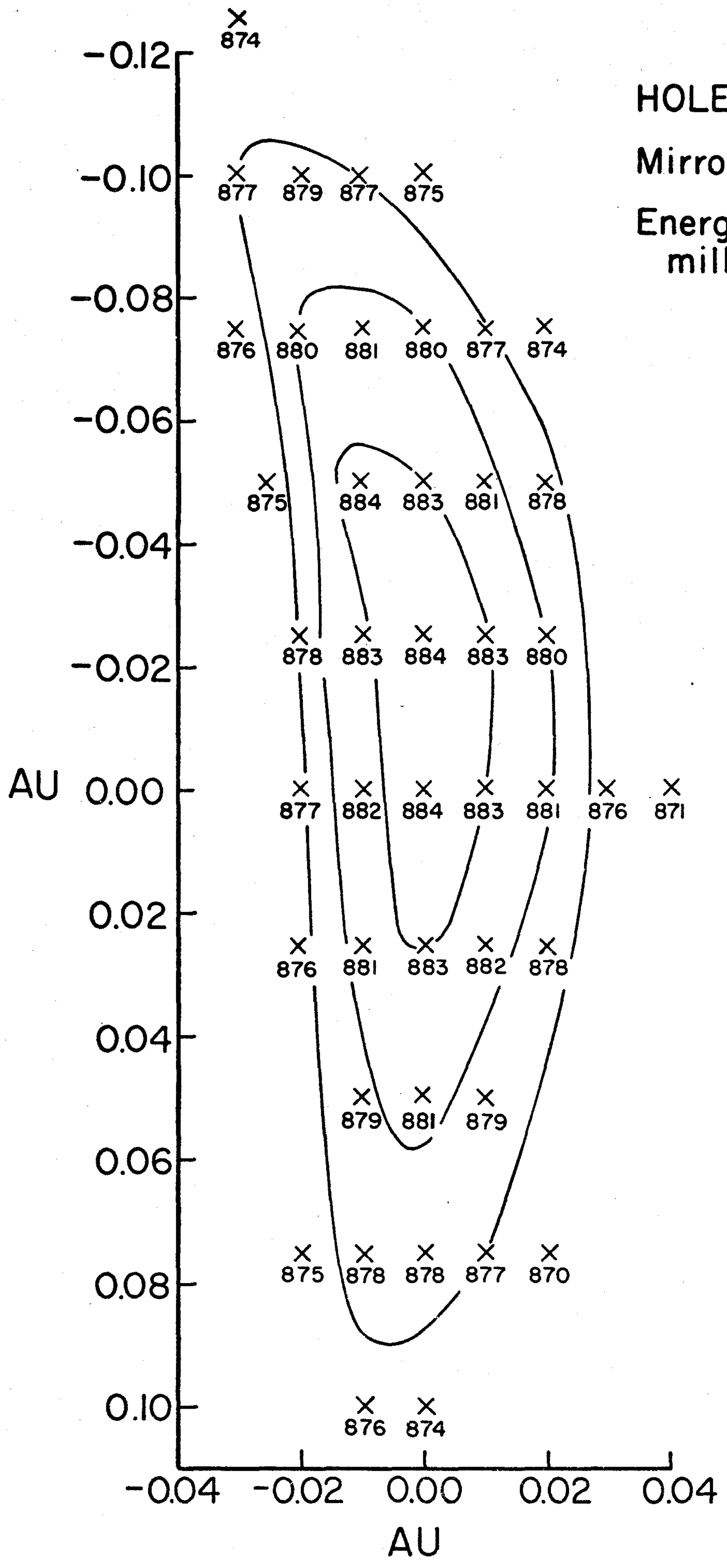

HOLES

Mirror Plane

Energy in
millirydbergs

Figure 18 Pseudopotential electron energy grid in the trigonal-binary mirror plane. Cut-off line is the Brillouin zone boundary.

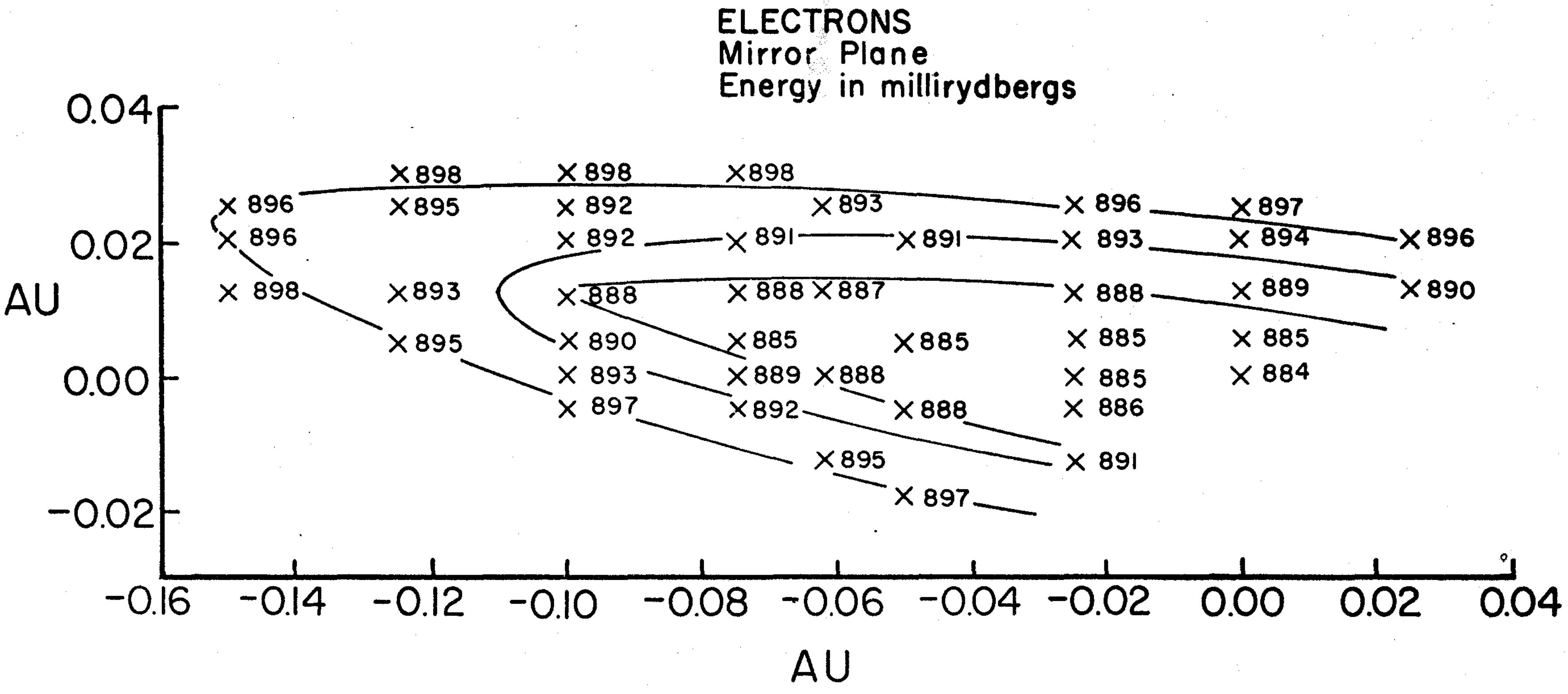
ELECTRONS
Mirror Plane
Energy in millirydbergs
0.04
0.02
0.00
−0.02
AU
−0.16
−0.14
−0.12
−0.10
−0.08
−0.06
−0.04
−0.02
0.00
0.02
0.04
AU
896
896
898
898
895
893
895
898
892
892
888
890
893
897
898
891
888
885
889
892
893
888
887
888
895
891
885
888
897
896
893
888
885
885
886
891
897
894
889
885
884
896
890

from symmetry while the hole maximum does not appear to be exactly at (0.0,00) - the H point. This happens because the H point has no special significance in the zone other than being a reference location near the center of the hole pocket. The energies are given in millirydbergs with respect to a band bottom of 0.000 Ry. The hole energy values include spin-orbit coupling to a nearby band with a spin-orbit constant of 0.02 Ry. Other grids parallel to the ones shown were obtained to describe the Fermi surface away from the mirror plane.

The contour lines indicate the shape of the Fermi surface with energy. Both surfaces are approximately ellipsoidal as expected. More exact comparisons were made by expanding the energy E in a power series in k up to fourth order and least squares fitting this series to the grid points. Using this series, cross-sectional areas and cyclotron masses were calculated numerically for any orientation. Fourteen parameters were used to describe the electron surface and twenty-two for the hole surface. The extremal hole surface areas are not central so a search was made for the maximum area corresponding to a dHvA frequency. The results are summarized in Table V. The Fermi energy E_F is referred to the band edge and concentrations are estimated from a comparison of the calculated minimum areas with the data. The alloy calculations were made by changing the Fermi energy to fit measured dHvA frequencies. This is using a rigid-band approach to alloying.

The choice of a Fermi energy is a problem in these

TABLE V

Results of a pseudopotential calculation of the Fermi surface of Sb and Sb(Sn) alloys

Trigonal-bisectrix plane-holes

est.conc. at.%	E_F Ry.	min. freq. (T)	max.freq. (T)	$\frac{m^*_{min}}{m}$	theor. max./min. freq.ratio	Observed max./min. freq. ratio
-.025	.003	57	248	.14	4.4	3.2
.23	.006	95	375	.13	4.0	2.8

Trigonal-bisectrix plane-electrons

est.conc. at.%	E_F Ry.	min. freq. (T)	max.freq. (T)	$\frac{m^*_{min}}{m}$	thecr. max./min. freq. ratio
0.00	.010	68.5	427	.073	6.2
.23	.006	37	234	.060	6.3

calculations. Since in pure antimony the number of electrons and holes are equal, a direct way of determining the Fermi energy is to search numerically for an energy giving equality of carriers. This cannot be done here since the spin-orbit splitting suppresses the hole band slightly below the electron band. This is a failing of either the pseudopotential or the spin-orbit calculation. However, a meaningful choice of Fermi energy in each band can be made by using a Fermi energy that correctly predicts one experimental value, in this case the minimum frequency and then using this energy to find the remaining undetermined frequencies and masses.

The theoretical hole surface does not describe the observed surface very well. The theoretical frequency ratios are too large making the calculated carrier density 25% too great. The calculated masses are twice the observed values and do not show much change with concentration. The model does predict a shape change of nearly the same percentage as found from the data.

The theoretical electron surface agrees more closely. The masses are nearly the observed size and show the downward trend with concentration found experimentally. The frequency ratio increases very slightly with concentration. In Falicov and Lin's (1966) paper, it was noted that the electron surface was described much better by the pseudopotential than was the hole surface. Part of this was attributed to the difficulties of calculation when the pocket has no inversion symmetry.

C. Non-rigid Bands

We have investigated some possibilities for non-rigid bands. The ellipsoidal parabolic model was used to estimate the band overlap energy E_o defined as the sum of the hole and electron Fermi energies. For non-rigid bands, E_o can change with concentration. E_o is constant within experimental error for all the alloys with a value of 0.016 Ry. It is interesting to compare this number with the values of 0.013 and 0.012 Ry. found from the two pseudopotential alloy calculations. The bands are rigid as found before.

The energy shifts of the centers of the pseudopotential bands were calculated allowing for changes of lattice constant and pseudopotential on alloying to check the rigid-band model in the pseudopotential calculation. The alloy lattice constants were taken from Table I except for the internal displacement parameter which was estimated for the alloys from the work of Morosin and Schirber (1969). The energy shifts were $\sim$ 0.0008 Ry/at % Sn. These are insignificant for concentrations of .25% or less.

A final comparison can be made with the scattering theory of Soven (1972). We have calculated the difference potential between the pseudopotentials of antimony and tin and estimated the s-wave phase shift δ_o from the Born approximation and from a numerical solution of the scattering equation

$$(-\frac{d^2}{dr^2} + V(r) - k^2)U_{o,k}(r) = 0 \quad .$$

Both give a value of $\delta_o \sim 0.1$. This number can be used with Soven's predictions for s and p wave scattering. Soven's results indicate that ∿ 80% of the rigid band energy shift should be expected for this value of δ_o. We find about 100% of the rigid band prediction. The difference is not surprising considering the assumptions made in the theory coupled with the problem of determining a pseudopotential difference accurately.

CHAPTER VIII

CONCLUSIONS

The hole and electron energy bands of pure antimony and antimony-tin alloys with up to 0.29 at % tin have been studied using the dHvA effect. At the highest concentration, the hole frequencies have increased by $\sim$ 75% over the pure antimony values while the electron frequencies have been reduced to less than half their original sizes. The cyclotron masses were found from the temperature dependence of the amplitude at the principal hole and electron branch minima. A Fourier transform method was used to separate the amplitudes of the different dHvA components. The hole mass increased by 35% while the electron mass decreased by nearly 32%. These mass changes are direct indications of nonparabolic conduction and valence bands. The Dingle temperature increases approximately linearly with concentration from the 2.5°K value of pure antimony to more than three times this value at .24 at % tin.

The rigid-band predictions without any corrections for changes of lattice parameter describe the observed frequency shifts quite well at low concentrations. At higher values there is a deviation caused by the mass and Fermi surface shape changes. Our data allow calculations of Fermi surface volumes and the corresponding electron and hole carrier densities. One tin atom removes one electron from the alloy as expected from the valence difference. This is different but more reasonable than that found by previous workers. If the electron carrier density is extrapolated to higher concentrations our results suggest that the electron pocket disappears at ∿ 0.35 at.% tin. A similar extrapolation for the holes implies that the hole band is empty at ∿ 0.35 at.% of a hexavalent element such as tellurium.

Various features of the data have been related to different band models. A Kane (1957) ellipsoidal nonparabolic band was used to describe the mass change with concentration. The $\overline{k}\cdot\overline{p}$ matrix element deduced from the data was 7.3 eV for holes and 5.0 eV for electrons. The mass and shape changes are compared with Falicov and Lin's (1966) band structure calculation in antimony. A fourth order expansion of the electron and hole surface was made from energy values found from diagonalizing an 89 x 89 pseudopotential determinant. The resulting functional form enabled the properties of the Fermi surface to be calculated. The electron band of the alloys is described much better by this model than is the hole band. A calculation based on the ellipsoidal parabolic model indicates that the band overlap is constant throughout our concentration range. An estimate of the scattering phase shift was found from the pseudopotential difference of antimony and tin and used to predict the deviation from rigid band behaviour as calculated by Soven (1972). The theoretical deviation was larger than that observed experimentally.

BIBLIOGRAPHY

Aurbach, R., Ketterson, J. B. and Windmiller, L. R., 1971, The Physics of Semimetals and Narrow-Gap Semiconductors, Dallas, ed. by D. L. Carter & R. T. Bate, (Pergamon), p. 41.

Barrett, C. S., Cucka, P. and Haefner, K., 1963, Acta Cryst. 16, 451.

Bowen, E. G. and Jones, W. M., 1931, Phil. Mag. 12, 441. These authors use a large unit cell defined by θ and a_L. α and a_R of the primitive rhombohedron are related to θ and a_L by the following formulae

$$e = \frac{2(1+\cos\theta-((2\cos\theta+1)(1-\cos\theta))^{1/2})}{3\cos\theta+1}$$

$$\cos\alpha = \frac{1+2e}{2+e^2}$$

$$a_R = a_L/(\frac{3e^2-4e+4}{2+e^2})^{1/2}$$

The lengths given in this paper are in KX ray units. 1 KXU = 1.002 Å.

Browne, S. H. and Lane, C. T., 1941, Phys. Rev. 60, 895.

Cohen, M. L. and Heine, V., 1970, Solid State Physics 24, 38.

1970a, ibid., pp. 196-216.

1970b, ibid., p. 53.

Datars, W. R. and Vanderkooy, J., 1964, IBM J. of Res. & Develop. *8*, 247. 247

Dresselhaus, M. S. and Mavroides, J. G., 1966, *Optical Properties and Electronic Structure of Metals and Alloys*, ed. by B. Abeles, (North Holland), Amsterdam, p. 508.

Ehrenreich, H., 1961, J. Appl. Phys. (Suppl.) *32*, 2155.

Ellett, M. R., Horst, R. B., Williams, L. R. and Cuff, K. F., 1966, *Proceedings of the International Conference on the Physics of Semiconductors*, Kyoto, J. Phys. Soc. Japan *21*, Suppl., 666.

Ellwood, E. C., Inst. Met. Ann. Eq. Diag. No. 23. Republished in Smithells (1967).

Epstein, S., 1962, J. Electrochem. Soc. *109*, 738.

Epstein, S. and Juretschke, A. J., 1963, Phys. Rev. *129*, 1148.

Everett, P. M., 1970, Cryogenics, *10*, 314.

Falicov, L. M. and Golin, S., 1965, Phys. Rev. *137*, A871.

Falicov, L. M. and Lin, P. J., 1966, Phys. Rev. *141*, 562.

Gold, A. V., 1968, *Solid State Physics, the Simon Fraser University Lectures, Vol. 1, Electrons in Metals*, ed. by J. F. Cochran and R. R. Haering, (Gordon and Breach), pp. 39-126.

1968a, ibid., pp. 113-114.

1968b, ibid., p. 115.

Hagg, G. and Hybinette, A. G., 1935, Phil. Mag. 20, 913. Lengths are given in KX ray units. 1KXU = 1.002 Å.

Hansen, M., 1958, Constitution of Binary Alloys, (McGraw-Hill), p. 1175.

Harrison, W. A., 1966, Pseudopotentials in the Theory of Metals, (W. A. Benjamin), New York.

1966a, ibid., p. 11.

1966b, ibid., p. 88.

1966c, ibid., pp. 79-86.

1966d, ibid., p. 143.

Heine, V., 1954, Proc. Phys. Soc. (London), A 69, 505.

Heine, V., 1970, Solid State Physics 24, 1.

Herod, R. D., Gage, C. A. and Goodrich, R. G., 1971, Phys. Rev. B 4, 1033.

Ishizawa, Y. and Tanuma, S., 1965, J. Phys. Soc. Japan 20, 1278.

Kane, E. O., 1957, J. Phys. Chem. Solids 1, 249.

Ketterson, J. B. and Windmiller, L. R., 1970, Phys. Rev. 1, 463.

Kittel, C., 1963, Quantum Theory of Solids, (J. Wiley & Sons), New York.

1963a, ibid., pp. 344-345.

Lax, B., Mavroides, J. G., Zeiger, W. J. and Keyes, R. J., 1960, Phys. Rev. Letters 5, 241.

Lifshitz, I. M. and Kosevich, A. M., 1955, Zh. Eksperim. i

Theor. Fiz. 29, 730 [English translation: Soviet Physics - JETP 2, 636 (1956)].

McCallum, D. C. and Taylor, W. A., 1967, Phys. Rev. 156, 782.

Morosin, B. and Schirber, J. E., 1969, Phys. Letters A 30, 512.

Nanney, C., 1963, Phys. Rev. 129, 109.

Pfann, W. G., 1966, Zone Melting, (J. Wiley & Sons), 2nd ed.

Poulsen, R. G., Moss, J. S. and Datars, W. R., 1971, Phys. Rev. B 3, 3107.

Ruby, S. L., Montgomery, H. and Kimball, C. W., 1970, Phys. Rev. B 1, 2948.

Saunders, G. A. and Oktu, O., 1968, J. Phys. Chem. Solids 29, 1589.

Smithells, C. J., 1967, Metals Reference Book, (Butterworth) 4th ed., Vol. 2, p. 567.

Soven, P., 1972, Phys. Rev. B 5, 260.

Tanuka, K., Susi, S. K. and Jain, A. L., 1968, Phys. Rev. 170, 664.

Weaire, D. and Williams, A. R., 1970, The Physics of Semimetals and Narrow-Gap Semiconductors, Dallas, ed. by D. L. Carter and R. T. Bate, (Pergamon), pp. 35-39.

Windmiller, L. R., 1966, Phys. Rev. 149, 472.

Wood, E. A., 1963, Crystal Orientation Manual, (Columbia University Press), New York, p. 75.

Zebouni, N. H. and Blewer, R. S., 1967, Phys. Letters A 24, 106.